Analytic Aerodynamic and Solar Radiation Pressure Modeling of Resident Space Objects

AE8900 MS Special Problems Report
Space Systems Design Lab (SSDL)
Guggenheim School of Aerospace Engineering
Georgia Institute of Technology
Atlanta, GA

Author:
Kenneth A. Hart, Jr.

Advisor:
Dr. Robert D. Braun

May 2, 2015

Analytic Aerodynamic and Solar Radiation Pressure Modeling of Resident Space Objects

Kenneth A. Hart,* and Robert D. Braun†

Georgia Institute of Technology, Atlanta, GA, 30332-1510, USA

Two significant non-gravitational perturbations on Earth-orbiting objects are aerodynamics and solar radiation pressure. An analytic methodology is developed to characterize these perturbations for primitive geometries. These results are validated against state of the art simulation techniques and observations. A superposition framework is developed to determine the perturbations for composite geometries. This framework is used to model the aerodynamic perturbations of a low orbiting nanosatellite. Analytic modeling of these perturbations can enable rapid trajectory and uncertainty propagation of Earth-orbiting objects.

Nomenclature

A	Area
C	Coefficient, see subscripts
c	Speed of light
D	Domain or drag, see context
$\boldsymbol{F}$	Force
H	Heaviside function
J	Jacobian determinant
Kn	Knudsen Number
l	Length
$\boldsymbol{M}$	Moment
$\boldsymbol{n}$	Surface normal vector
q	Dynamic pressure
R	Specific gas constant
$\boldsymbol{r}$	Surface parameterization
r	Radius
$\boldsymbol{S}$	Solar vector
s	Molecular speed ratio
T	Temperature
$\boldsymbol{t}$	Surface tangent vector
u	First surface parameterization variable
$\boldsymbol{V}$	Velocity or volume, see context
v	Second surface parameterization variable

Subscripts

a	Aerodynamic
c	Cone
char	Characteristic
F	Force
M	Moment

---

*Graduate Research Assistant, Daniel Guggenheim School of Aerospace Engineering, AIAA Student Member.
†David & Andrew Lewis Professor of Space Technology, Daniel Guggenheim School of Aerospace Engineering, AIAA Fellow.

American Institute of Aeronautics and Astronautics

N	Normal
p	Pressure
s	Solar radiation pressure
T	Tangential
W	Wall
w	Wetted

Symbols

α	Angle of attack
∞	Freestream
β	Sideslip angle or solar incidence angle, see context
δ	Half angle or diffusivity, see context
$\odot$	Solar
θ	Freestream incidence angle
λ	Mean free path
ρ	Reflectivity
σ	Accommodation coefficient, see subscripts
τ	Shear
Φ	Flux
ϕ	Flap angle
Ω	Surface

I.   Introduction

THE recent collision between two satellites and Chinese anti-satellite demonstration have motivated improvements to space situation awareness. The space industry is valued at an estimated \$314 billion and in-space assets share Earth orbits with decommissioned satellites and other potentially hazardous space debris.[1] Accurate knowledge of and quantified uncertainty in the orbits of all resident space objects (RSOs) must be maintained in order to minimize the probability of future collisions.[2] To predict whether any two of the 20,000 tracked objects will collide, ground-based observations of the objects can be synthesized with accurate models of the dynamics of each object. These dynamics models include the Earth's gravity field and the non-gravitational perturbations of solar radiation pressure (SRP) and atmospheric drag.

Many objects in the Space Catalog receive significant perturbing forces due to Earth's atmosphere, which produces aerodynamic forces that act on these bodies. Similarly, satellites in higher altitude orbits such as geosynchronous satellites are perturbed by pressure from the Sun's radiation. The magnitude of these perturbations can be determined by analytical modeling, numerical simulations, or experimental testing. Numerical and experimental data are often more accurate than analytical models, however run times become problematic with many thousands of objects. Since many RSOs are partially resolvable from ground-based observations, knowledge of their geometry would change over time, necessitating updates to aerodynamic and SRP databases. These solutions cannot practically be coupled with rapid RSO trajectory propagation tools.

A fast and flexible alternative is to analytically model the perturbations. The models are equations that express the forces and moments as functions of the geometry and orientation of the object, as well as other aerodynamic and optical properties. Recently high-fidelity, analytical expressions for hypersonic aerodynamics have been developed for a general range of shapes and these have enabled fast propagation of trajectories for various range of vehicles in the hypersonic regime.[3–5] Although these methods were originally developed for hypersonic continuum flow, the general methodology can be extended to rarefied aerodynamics and SRP.

A.   Overview

The analytic models for the infinitesimal forces due to rarefied aerodynamics and to SRP are detailed and applied to a variety of primitive geometries. A general framework for combining these geometries is described and applied to fundamental axisymmetric shapes. The resulting analytic expressions for rarefied aerodynamics are compared against experimental data and direct simulation Monte Carlo results and the solar radiation expressions are compared against panel approximations of the geometries. The analytic model

for rarefied aerodynamics is applied to a case study on a nanosatellite in low Earth orbit.

II. Background

A. Rarefied Aerodynamics

1. Flow Properties

In general, aerodynamic forces and moments arise from the momentum transferred from a fluid to an object submerged in that fluid. Fluid flows in a manner which conserves three fundamental quantities: mass, momentum, and energy.[6] All fluid flows are governed by the Boltzmann equation, which is a recasting of the three conservation laws and treats all fluids as a system of particles. The Boltzmann equation is more appropriate than the well-known Navier-Stokes equations in fluid flows about orbiting satellites due to the relatively low density of the fluid and high speeds required to maintain orbit. The regime of flows experienced by RSOs is generally a rarefied flow, meaning that the density of molecules is so low that the gas no longer behaves like a continuum. Since Navier-Stokes only applies for continuum flows, it cannot be applied in the rarefied regime and the Boltzmann equation governs the flow.

Traditionally, free-molecular flow theory is based upon the assumption that the flow incident on the body is independent of any effect of the particles reemitted from the surface of the body after collision.[7] Hence, the incident flow is entirely undisturbed by the presence of the body.[8] Though much of the literature rests on this assumption,[7–10] there have been investigations into cases where reemitted particles collide with the surface of the body more than once.[11,12] The similarity parameter that is generally used to define the interfaces between continuum flow, rarefied flow, and the regime between them known as transition flow, is the Knudsen Number (Kn) of the flow. This dimensionless quantity is defined in Eq. (1) as the ratio between the mean free path of the gas (λ) and the characteristic dimension (l_{char}) of the object submerged in the gas. So long as the Knudsen Number of a flow exceeds a value of 10, the flow regime is considered rarefied.[8] For reference, a 1U (10 cm × 10 cm × 10 cm) nanosatellite will experience rarefied flows at altitudes above approximately 100 km on the Earth.[6]

$$\text{Kn} = \frac{\lambda}{l_{\text{char}}} \tag{1}$$

A high Knudsen Number is characteristic of rarefied flow, while low Knudsen number is characteristic of continuum flow. Figure 1(a) shows the expected Knudsen numbers and the flow type for a 1-m-long vehicle at different altitudes.[6] Based on the Knudsen number classification shown in the figure, the high altitude region where most RSO orbits reside is characterized by free-molecular flow.


(a) Knudsen number vs. altitude for a 1-m-long object.[6]   (b) Flow behavior from free-molecular to continuum.[13]
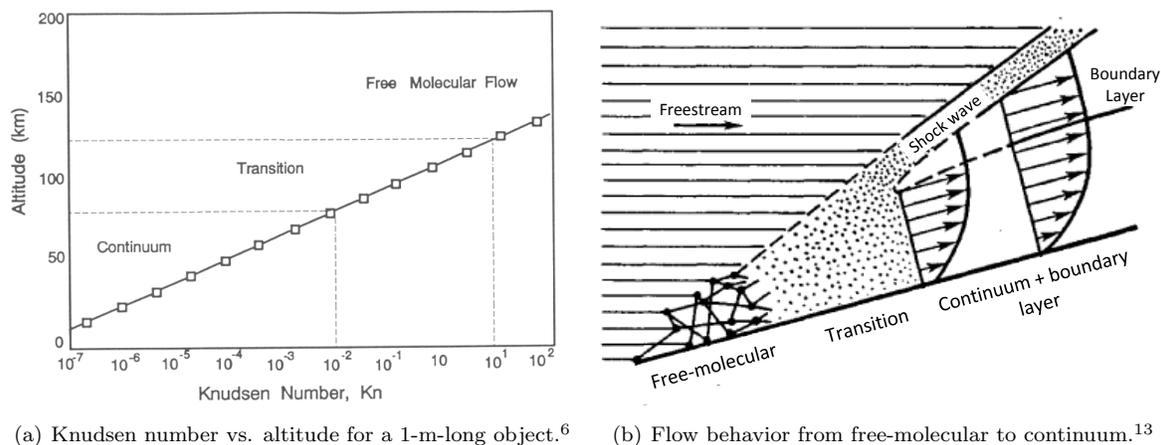
Figure 1. Schematic of Free-molecular regime flow and its extent in atmosphere.

Free-molecular flow is a regime characterized by extreme rarefaction of the atmosphere. A molecule can travel long distances (relative to the characteristic length of the body) without collisions. Additionally, it can be assumed that the flow incident on the body is independent of any effect of the particles reemitted from the surface of the body after collision. Hence, the incident flow is entirely undisturbed by the presence

American Institute of Aeronautics and Astronautics

of the body.[8] Figure 1(b) shows a schematic of flow in the free-molecular regime and also describes the transition from free-molecular to continuum flow. Although the figure is not to scale, it is descriptive of the free molecular flow and one can see that neither shock waves nor boundary layers have any effect on the flow incident on the body in free-molecule flow.[8]

2. Modeling Techniques

An accepted model for the coefficients of shear and pressure on a panel in rarefied flow are the Schaaf & Chambré model given by Eqs. (2) and (3).[8] The molecular speed ratio is defined in Eq. (4) as the ratio between the freestream velocity and the thermal velocity of the gas. In this equation, $|| \cdot ||$ is the Euclidean norm. The pressure and shear coefficients for a flat plate derived by Schaaf & Chambré has been extended to curved surfaces by considering an infinitesimal element of area.[10, 14–16]

$$
C_p = \frac{1}{s^2} \left[\left(\frac{2 - \sigma_N}{\sqrt{\pi}} s \sin\theta + \frac{\sigma_N}{2} \sqrt{\frac{T_w}{T_\infty}} \right) e^{-(s\sin\theta)^2} \right.
$$
$$
\left. + \left\{ (2 - \sigma_N) \left((s\sin\theta)^2 + \frac{1}{2} \right) + \frac{\sigma_N}{2} \sqrt{\frac{\pi T_w}{T}} s \sin\theta \right\} (1 + \mathrm{erf}(s\sin\theta)) \right]
\tag{2}
$$

$$
C_\tau = -\frac{\sigma_T \cos\theta}{s\sqrt{\pi}} \left[e^{-(s\sin\theta)^2} + \sqrt{\pi} s \sin\theta \left(1 + \mathrm{erf}(s\sin\theta) \right) \right]
\tag{3}
$$

$$
s = \frac{||\boldsymbol{V}_\infty||}{\sqrt{2RT_\infty}}
\tag{4}
$$

$$
d\boldsymbol{F}_a = q_\infty \left(C_p \hat{\boldsymbol{n}} + C_\tau \hat{\boldsymbol{t}} \right) dA
\tag{5}
$$

The properties of the reflected molecules can be highly problem-dependent and can be characterized in terms of accommodation coefficients. The normal momentum accommodation coefficient (σ_N) describes the change in normal momentum due to the molecular-surface interaction, while the tangential momentum accommodation coefficient (σ_T) describes the momentum change in the tangential direction. These quantities are described in Eqs. (6) and (7).[8] Note that p is pressure (normal to the surface) and τ is the shear pressure and they designate conditions of the incident molecules (subscript i), the reflected molecules (subscript r), or the wall (subscript w). Represented values σ_N and σ_T can be found in found in Ref. 17. Specular reflection simplifies to $\sigma_N = \sigma_T = 0$, while diffuse reflection is $\sigma_N = \sigma_T = 1$.[6]

$$
\sigma_N = \frac{p_i - p_r}{p_i - p_w}
\tag{6}
$$

$$
\sigma_T = \frac{\tau_i - \tau_r}{\tau_i}
\tag{7}
$$

The equations for pressure and shear coefficients can be simplified from Eqs. (2) and (3) to enable analytic integration over curved surfaces. The most common simplification is the application of the hyperthermal limit, which is the limit as s approaches infinity.[6, 7, 9] In some cases the limit is applied throughout, resulting in the simplified expressions found in Regan; in others the limit is only applied to eliminate the exponential and error function terms. For large values of s, the exponential terms decay to zero while the error function approaches unity.

B. Solar Radiation Pressure

1. Force on a Plate

The force due to SRP on a flat plate can be derived analytically by assuming that the surface behaves like a linear combination of a black body, a perfect mirror, and a Lambert diffuser.[18] In other words, the absorption, reflection, and diffusion coefficients completely specify the optical properties of the surface and they are independent of the angle of incidence, direction, and wavelength. The infinitesimal force at a point is adapted from Milani in Eq (8). Coincidentally, this model has the same functional form as the force model

American Institute of Aeronautics and Astronautics

for a hyperthermal rarefied flow, which follows a sine-squared law in the normal direction and a sine-cosine law in the tangential direction.[6]

$$d\boldsymbol{F}_s = -\frac{\Phi_\odot}{c}\left[2\left(\frac{\delta}{3}\cos\beta + \rho\cos^2\beta\right)\hat{\boldsymbol{n}} + (1-\rho)\cos\beta\,\hat{\boldsymbol{S}}\right]dA \tag{8}$$

2. Solar Flux Modeling

The primary scale factor for the force due to SRP is the solar flux, $\Phi_\odot$. A good approximation for the value of the solar flux is total solar irradiance (TSI), which is defined as the total energy output from the Sun per unit time per unit area at a distance of 1 AU from the Sun. This value is approximately 1367 W/m^2, within 1%.There are several methods for improving the model of solar flux, including an inverse-square law, a sinusoidal solar cycle, and ramping the solar flux through Earth's penumbra.[19] Since the Sun's output is variable on the timescale of hours, all efforts to model $\Phi_\odot$ will include some degree of uncertainty. For all objects with length scale significantly less than 1 AU, solar flux will be constant across the object. Since this applies to all objects orbiting the Earth, $\Phi_\odot$ is treated as a constant with respect to surface integration. Rather than replacing the solar flux with a model, it is left symbolic in this investigation so that any model can be applied. The solar flux can also be treated as a random variable in the context of uncertainty propagation. In this formulation, the forces and moments are SRP multiplied by area and volume vectors, respectively.

III. Analytic Methodology

In Section II, analytic models of the force due to rarefied aerodynamics and to SRP are derived for flat plates. The area of this plates can be scaled down to an infinitesimal, shown in Figure 2(a), to describe the force at a point. These infinitesimals can be integrated to describe the rarefied aerodynamics and solar radiation perturbation forces and moments on an object with a regularly parameterized surface. There are two aspects of this integration process: the integrand and the domain of integration. This process is the same for both perturbations, so for brevity the process is described once for the case of rarefied aerodynamics. This formulation has been applied in previous analytic hypersonic aerodynamics investigations for both the rarefied and continuum regimes.[3–5, 10, 16] To apply this methodology to solar radiation pressure, C_p is replaced by f_p and C_τ is replaced by f_τ. Additionally, the integrals are scaled by solar radiation pressure instead of scaling by A_{ref} and l_{ref}.

(a) Aerodynamic Model   (b) SRP Model
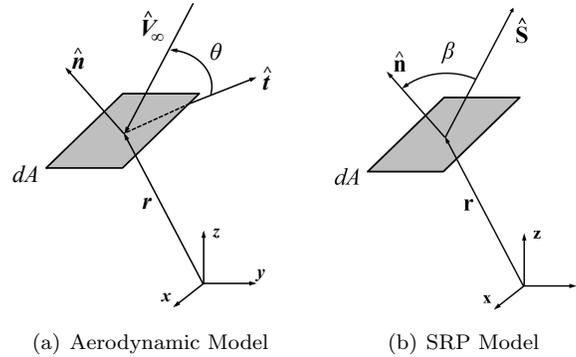
Figure 2. Vector diagrams for the two perturbation models.

A. Formulation of the Integrand

The integrands in this methodology are the infinitesimal contributions to the aerodynamic coefficients and the SRP perturbations. This vector quantity is resolved into components normal and tangential to the surface. Though there are infinitely many vectors tangential to the surface, the tangential vector is specified by projecting the freestream velocity and the solar vectors onto the tangent plane. A surface parameterized by the variables u and v in the domain D as in Eq. (9) has a normal vector is given by Eq. (12). The surface

American Institute of Aeronautics and Astronautics

does not need to be regular, so long as there are a finite number of points where the partials in Eq. (10) are parallel.

$$r : D \subset \mathbb{R}^2 \to \mathbb{R}^3 \tag{9}$$

$$n = \frac{\partial r}{\partial u} \times \frac{\partial r}{\partial v} \tag{10}$$

$$J = \|n\| \tag{11}$$

$$\hat{n} = \frac{n}{J} \tag{12}$$

The freestream and solar vectors are given in Eqs. (13) and (14) by the Euler angle rotation of the first body axis towards the freestream and the Sun, respectively. The classical Euler angles are subscripted to indicate that, for an arbitrary orientation, the freestream and solar vectors are not linearly dependent. In the SRP model, the symbol β is used both to describe the solar beta angle, as in Figure 2(b) and the second Euler angle as in Eq. (14). Without a subscript, the symbol indicates the solar beta angle.

$$\hat{V}_\infty = - \begin{bmatrix} \cos \alpha_a \cos \beta_a & \sin \beta_a & \sin \alpha_a \cos \beta_a \end{bmatrix}^\mathsf{T} \tag{13}$$

$$\hat{S} = \begin{bmatrix} \cos \alpha_s \cos \beta_s & \sin \beta_s & \sin \alpha_s \cos \beta_s \end{bmatrix}^\mathsf{T} \tag{14}$$

$$\sin \theta = -\hat{V}_\infty \cdot \hat{n} \tag{15}$$

$$\cos \beta = \hat{S} \cdot \hat{n} \tag{16}$$

$$\hat{t}_a = \frac{1}{\cos (\theta)} \left[\hat{n} \times \left(-\hat{V}_\infty \times \hat{n} \right) \right] \tag{17}$$

The infinitesimal models in Eqs. (2)-(3) and (8) and the vector and dot product definitions in Eqs. (12) - (17) are the components required to generate the integrands for rarefied aerodynamics and SRP.

B. Domain of Integration

The surface Ω parameterized by r as in Eq. (9) has a domain, D, of (u, v) pairs that map onto the surface. That domain in $\mathbb{R}^2$ is split into two disjoint subsets: the wetted and shadowed regions of the surface. This distinction is important because the entire surface does not see the freestream or the sun, in general. The wetted region is defined in Eqs. (21) and (22) by the locus of (u, v) pairs in D where the freestream or solar vector is above the local horizon.

$$\Omega = \{ r : (u, v) \in D \} \tag{18}$$

$$D_{w,a} = \{ (u, v) : (u, v) \in D \wedge \sin \theta \geq 0 \} \tag{19}$$

$$D_{w,s} = \{ (u, v) : (u, v) \in D \wedge \cos \beta \geq 0 \} \tag{20}$$

$$\Omega_{w,a} = \{ r : (u, v) \in D_{w,a} \} \tag{21}$$

$$\Omega_{w,s} = \{ r : (u, v) \in D_{w,s} \} \tag{22}$$

To implement these definitions of the wetted region requires changing the limits of integration. The dot products given in Eqs. (15) and (16) can be set to zero to obtain an implicit function of (u, v) pairs that lie on the shadow boundary. For most surface geometries, this implicit equation can be rearranged to isolate one of the parameterization variables. If it cannot be rearranged to isolate one of the variables, an alternative parameterization of the surface may yield a separable equation for the shadow boundary. For example, a stereographic projection of the sphere a circular domain of integration, which is more well-behaved than the expression in spherical coordinates. After isolating one of the parameterization variables, this expression can be incorporated into the limits of integration to restrict the domain to the wetted region. Which limit of integration is replaced depends on the sign of incidence angles, and a test point can be used as a check.

American Institute of Aeronautics and Astronautics

C. Surface Integral Formulation

The expressions for the integrands in Eqs. (5) and (8) and the domains of integration in Eqs. (19) and (20) are the two pieces of information required to generate the surface integral definitions for the aerodynamic and solar perturbations on RSOs. Combining them results in Eqs. (23) and (24), describing the aerodynamic forces and moments, and Eqs. (27) and (28) describing the forces and moments due to SRP.

$$\boldsymbol{F}_a = q_\infty \iint\limits_{D_{w,a}} \left(C_p \hat{\boldsymbol{n}} + C_\tau \hat{\boldsymbol{t}} \right) dA \tag{23}$$

$$\boldsymbol{M}_a = q_\infty \iint\limits_{D_{w,a}} \boldsymbol{r} \times \left(C_p \hat{\boldsymbol{n}} + C_\tau \hat{\boldsymbol{t}} \right) dA \tag{24}$$

$$\boldsymbol{C}_F = \frac{\boldsymbol{F}_a}{q_\infty A_{ref}} \tag{25}$$

$$\boldsymbol{C}_M = \frac{\boldsymbol{M}_a}{q_\infty A_{ref} l_{ref}} \tag{26}$$

$$\boldsymbol{F}_s = -\frac{\Phi_\odot}{c} \iint\limits_{D_{w,S}} \left[2 \left(\frac{\delta}{3} \cos\beta + \rho \cos^2\beta \right) \hat{\boldsymbol{n}} + (1-\rho) \cos\beta \, \hat{\boldsymbol{S}} \right] dA \tag{27}$$

$$\boldsymbol{M}_s = -\frac{\Phi_\odot}{c} \iint\limits_{D_{w,S}} \boldsymbol{r} \times \left[2 \left(\frac{\delta}{3} \cos\beta + \rho \cos^2\beta \right) \hat{\boldsymbol{n}} + (1-\rho) \cos\beta \, \hat{\boldsymbol{S}} \right] dA \tag{28}$$

$$\boldsymbol{A}_s = -\frac{c}{\Phi_\odot} \boldsymbol{F}_s \tag{29}$$

$$\boldsymbol{V}_s = -\frac{c}{\Phi_\odot} \boldsymbol{M}_s \tag{30}$$

The coefficients in Eqs. (25) and (26) and the SRP multipliers in Eqs. (29) and (30) are the integral terms in the force and moment equations. The coefficients and multipliers are independent of the freestream dynamic pressure and the solar radiation pressure, which can be determined with separate models of the atmosphere and the solar cycle.

D. Application of the Heaviside Function

The Heaviside function provides an alternative implementation of the shadow boundary compared to Eqs. (19) and (20). For some geometries, the shadow boundary may not be separable and introduced into the domain of integration, as described in Section B. In this case, the integral forms shown in Eqs. (31)-(32) would be more valuable.

$$\iint\limits_{D_{w,a}} d\boldsymbol{F}_a = \iint\limits_{D_a} H\left(\sin\theta\right) d\boldsymbol{F}_a \tag{31}$$

$$\iint\limits_{D_{w,s}} d\boldsymbol{F}_s = \iint\limits_{D_s} H\left(\cos\beta\right) d\boldsymbol{F}_s \tag{32}$$

Introducing the Heaviside function shifts the shadow constraint handling from the domain of integration to the integrand itself. It can be applied to both force and moment equations. This improves performance of a finite-difference numerical integration scheme and can enable analytic expressions for piecewise parameterized surfaces. For other surfaces, such as spheres and ellipsoids, the Heaviside function can complicate the analytic integration process if the argument is a function of the two parameterization variables.

E.   Superposition Framework

The geometries presented in the previous section are good first-order approximations to the shape of RSOs, however these shapes could be combined for greater geometric fidelity. In combining the shapes, two phenomena are possible: self-reflection and self-shadowing. Self-reflection occurs when molecules of air or photons of light can collide with the surface more than once. Self-shadowing occurs when a force is not acted on a part of the surface oriented towards the flow or the Sun because it is in the shadow of another surface. This investigation focused on the phenomenon of self-shadowing because its incorporation into the model requires manipulation of the limits of integration. The incorporation of self-reflection has been achieved in restricted cases and specialized re-derivation of the infinitesimal force models was required.[11,12] For these reasons, the following derivations incorporated only self-shadowing into the superposition framework.
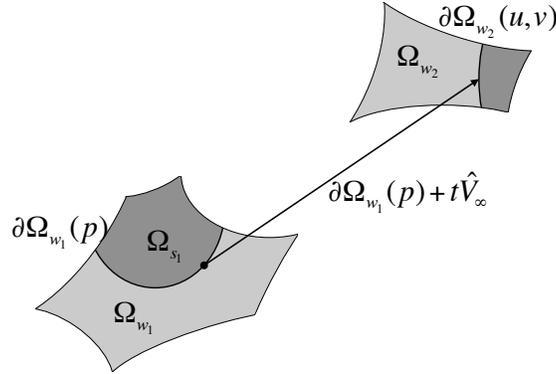

Figure 3. Map of the shadow from one surface onto another.

Piecewise surfaces which are locally convex but globally concave exhibit self-shadowing, where part of the surface could be invisible to the flow despite being oriented toward it. To map the shadow from one surface onto another, the locus of shadowed points on the first surface are transported along the freestream vector to the second surface. This defines a curve on the second surface which represents the boundary of the shadow. This process is illustrated in Figure 3. Which side of the curve the interior of the shadow maps to can be determined by testing a value within the shadow of the first surface and determining where it maps to on the second surface. The system of three equations in Eq. (33) has four unknowns: a coordinate, p, along $\partial\Omega_{w_1}$, the parameters u and v of Ω_2, and an arbitrary variable t that scales the freestream vector. These three equations, one for each entry in the position vector, are shown graphically in Figure 3 and mathematically in Eq. (33). From these three equations, a relationship between u and v on Ω_2 is derived to define the shadow boundary.

$$\partial\Omega_{w_2}(u, v) = \partial\Omega_{w_1}(p) + t\hat{\mathbf{V}}_\infty \qquad (33)$$

The expression in Eq. (33) is an analytic raytracing technique that can be applied in reverse to determine the boundary on Ω_1 of the shadow from Ω_2. Any number of surfaces can be included in a model, and in general for n independent surfaces there are $n(n-1)$ shadowing combinations. Topologically, this is an all-to-all bidirected graph where the nodes are the surfaces and the edges are the shadows. In the axisymmetric applications below, there are substantially fewer than $n(n-1)$ shadowing combinations. For example, the stepped cylinder has 5 unique parameterized surfaces but only 2 shadowing combinations. This sparseness is due to the fact that shadowing is not mathematically possible in many cases, like the circular panel on the front of the stepped cylinder cannot shadow the circular panel on the back. In any case where there are multiple shadows on one surface, the domain of integration becomes all points in D which are neither in the surface's natural shadow nor in the union of the shadows from other surfaces. The ith domain of integration for a model composed of n surfaces can be expressed by Eq. (34). Since the integral is a linear operator, the sum over all the unique surfaces can be moved outside of the integral as shown in Eq. (35). This technique is applied to derive analytic expressions for the aerodynamic and SRP disturbances of composite geometries.

$$D_{w_i} = \left\{ (u, v) : (u, v) \notin \bigcup_{j \in \{1, 2, ..., n\}} D_{s_{j \to i}} \right\} \qquad (34)$$

American Institute of Aeronautics and Astronautics

$$\iint\limits_{D_w} d\boldsymbol{f} = \sum_{i=1}^{n} \iint\limits_{D_{w,i}} d\boldsymbol{f}_i \tag{35}$$

IV. Geometries

A. Primitive Geometries

Geometric primitive is a term borrowed from the computer graphics industry to describe the most basic solid shapes. Common primitives include the cube, cylinder, sphere, and cone. Through scaling operations, the cube and the sphere become a cuboid and an ellipsoid, respectively. For a surface to be considered primitive, it must be compact, orientable, and without boundary and satisfy the condition that the surface is globally convex. In other words, there is no $p \in \Omega$ such that the points in a neighborhood about p are hyperbolic. Graphics engines include the torus as a primitive, however it does not satisfy this condition.[20] Analytic expressions are developed for the cuboid, cylinder, cone, and ellipsoid geometric primitives. The properties of these shapes, including the specifications of the shapes used for validation, are detailed in the following sections.

1. Cuboid

The cuboid is a polyhedron composed of three pairs of rectangular faces placed opposite each other and joined at right angles.[20] The cuboid, like the ellipsoid, can approximate a wide variety of geometries through its three parameters. A cuboid is specified by the lengths of the the three edges: l_x, l_y, and l_z, as shown in Figure X. To generate analytic expressions for the perturbations on a cuboid, the flat plate equations are applied for each face and the Heaviside formulations in Eq. (31) is applied to switch off the faces that are shadowed. This formulation is similar to a panel code, though it differs in that analytic expression does not include a for loop or if statements.[6] For a cuboid, the reference area is defined by the $y - z$ cross-sectional area, $l_y l_z$, and the reference length is defined as l_x. Both expressions for moments on the cuboid are taken about the geometric center.

2. Cylinder

The cylinder, specifically a right circular cylinder, is a solid bounded by a closed, right, circular cylindrical surface and two planes. This is the most common use of the term, though it can also be used for non-circular cylinders and cylinders with cross sections that are not perpendicular to the axis.[20] Two dimensions define a cylinder: its radius r and length l. In the aerodynamic expressions, the reference area is the cross-sectional area of the cylinder, πr^2, and the reference length is l. The moments are taken about the geometric center of the cylinder. In simulations, a cylinder of diameter A and length B, shown in Figure X, was used for validation. Because the cylinder is rotationally symmetric about the x-axis and the y-z plane is a plane of symmetry, integration over the surface of a cylinder is greatly simplified. The two circular plates at the ends of the cylinder are incorporated with the Heaviside formulation.

3. Cone

The right circular cone is constructed from the locus of rays from a point to a circle, where the line between the center of the circle the vertex is normal to the circle. Rarefied aerodynamics of the cone and other nosecone geometries were studied extensively during the Cold War, though primarily restricted in their applicability to the case where the total angle of attack is less than the cone angle.[8] Analytic expressions for the perturbations on the cone can be manipulated to generate the aerodynamics of a conical frustum by the first fundamental theorem of calculus. Two parameters that fully specify a cone are the cone angle, δ_c, and the base radius r_c as shown in Figure X. The aerodynamic reference area and length for the cone are πr_c^2 and $r_c \cot \delta_c$, respectively, and the moments are taken about the vertex of the cone. Numerical simulations on a cone with a cone angle of X degrees and base radius of Y are performed for validation. Since the cone is rotationally symmetric about the x-axis, the analytic integration is greatly simplified. To enable analytic expressions of the aerodynamic coefficients, the hyperthermal limit was partially applied to the Schaaf & Chambré model, eliminating the exponential and error function terms.

American Institute of Aeronautics and Astronautics

4. Ellipsoid

An ellipsoid is a solid, equivalent to a sphere that has been scaled in three orthogonal directions. It is similar to the cuboid in that the three radii, r_x, r_y, and r_z can be varied to produce an array of shapes. As shown in Figure X, these radii correspond to the semi-principal axes of the ellipsoid. (include sentence about previous attempts) To obtain the rarefied aerodynamic coefficients for the ellipsoid, the full hyperthermal limit is applied and the surface is parameterized by stereographic projection. The ellipsoid has three planes of symmetry, reducing the range of freestream and solar vector orientations required for validation. In the expressions for the rarefied aerodynamics, the reference area and length are $\pi r_y r_z$ and r_x and for both moment expressions the moments are taken about the geometry center of the ellipsoid. An ellipsoid with radii $(5, 2, 1)$ was used to validate the analytic expressions.

B. Composite Geometries

(a) Stepped Cylinder

(b) Increasing Biconic

(c) Decreasing Biconic

(d) Mars Microprobe Aeroshell[21]
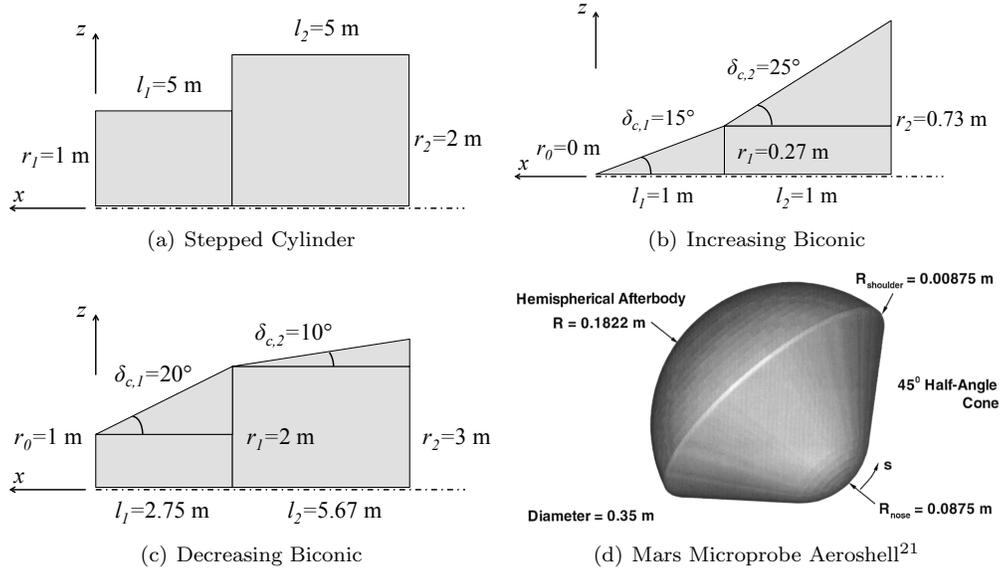
Figure 4. Validation geometries for analytic aerodynamic coefficients.

1. Stepped Cylinder

The stepped cylinder, shown in Figure 4(a), is geometrically defined by two non-intersecting coaxial cylinders joined at their planar surfaces. The geometry is axisymmetric, so the derivation of the aerodynamic coefficients assumes that the freestream velocity is in the x-z plane shown in Figure 4(a). This configuration has 5 parameterized surfaces: the forward panel, the forward cylindrical hull, the center panel, the aft cylindrical hull, and the aft panel. The parameterizations for these surfaces are given by Eqs. (36)-(40). It is assumed that the aft radius is greater than the forward radius for simplicity, since the converse can be handled by reversing the freestream direction.

$$\mathbf{r}_{\text{forward panel}} = \begin{bmatrix} 0, & u_1 \sin v_1, & u_2 \cos v_1) \end{bmatrix}^{\mathsf{T}} \qquad u_1 \in [0, r_1], v_1 \in [-\pi, \pi] \qquad (36)$$

$$\mathbf{r}_{\text{forward hull}} = \begin{bmatrix} -u_2, & r_1 \sin v_2, & r_1 \cos v_2 \end{bmatrix}^{\mathsf{T}} \qquad u_2 \in [0, l_1], v_2 \in [-\pi, \pi] \qquad (37)$$

$$\mathbf{r}_{\text{middle panel}} = \begin{bmatrix} -l_1, & u_3 \sin v_3, & u_3 \cos v_3 \end{bmatrix}^{\mathsf{T}} \qquad u_3 \in [r_1, r_2], v_3 \in [-\pi, \pi] \qquad (38)$$

$$\mathbf{r}_{\text{aft hull}} = \begin{bmatrix} -l_1 - u_3, & r_2 \sin v_4, & r_2 \cos v_4 \end{bmatrix}^{\mathsf{T}} \qquad u_4 \in [0, l_2], v_4 \in [-\pi, \pi] \qquad (39)$$

$$\mathbf{r}_{\text{aft panel}} = \begin{bmatrix} -l_1 - l_2, & v_5 \sin u_5, & v_5 \cos u_5 \end{bmatrix}^{\mathsf{T}} \qquad u_5 \in [-\pi, \pi], v_5 \in [0, r_2] \qquad (40)$$

The shadow on the center panel created by the forward cylinder is the shadow of a cylinder constrained by a circular boundary. The boundary of this shadow would be a complex piecewise function, however this is entirely unnecessary. Since the elemental forces are constant across a panel, it is sufficient to find the area

American Institute of Aeronautics and Astronautics

of the shadow then subtract that area from the area of the center panel. Solving for this area is a matter of geometry, and the results are provided below.

$$A_w = \pi r_2^2 - \begin{cases} 2l_1 r_1 \tan(\alpha) + \pi r_1^2 & l_1 \tan(\alpha) \leq r_2 - r_1 \\ \begin{aligned} 2l_1 r_1 \tan(\alpha) + \pi r_1^2 \\ -2\Delta - r_1^2 \sec^{-1}\left(\frac{2l_1 r_1 \tan(\alpha)}{-l_1^2 \tan^2(\alpha) - r_1^2 + r_2^2} \right) \\ +r_2^2 \sec^{-1}\left(\frac{2l_1 r_2 \tan(\alpha)}{l_1^2 \tan^2(\alpha) - r_1^2 + r_2^2} \right) \end{aligned} & r_2 - r_1 < l_1 \tan(\alpha) \leq \sqrt{r_2^2 - r_1^2} \\ \frac{\pi r_1^2}{2} + r_1\sqrt{r_2^2 - r_1^2} + r_2^2 \sin^{-1}\left(\frac{r_1}{r_2} \right) & \sqrt{r_2^2 - r_1^2} < l_1 \tan(\alpha) \end{cases} \tag{41}$$

$$\Delta = \frac{1}{4}\sqrt{(-l_1 \tan(\alpha) + r_1 + r_2)(l_1 \tan(\alpha) + r_1 - r_2)(l_1 \tan(\alpha) - r_1 + r_2)(l_1 \tan(\alpha) + r_1 + r_2)} \tag{42}$$

The complexity of this formula for the wetted area of the center panel is due to calculation of the lune between the edge of the panel and the edge of the shadow. In the case where the radii are significantly different in scale, then the second expression could be eliminated without a significant loss of fidelity. This would not be the case if the cylinders were approximations of a solid of revolution, so the lune area calculation is kept for completeness. Including the effect of self-shadowing from a cylinder onto a panel is accomplished by subtracting the area of the shadow from the total area of the panel.

When the freestream velocity forms an obtuse angle with the x-axis, the center panel shadows the forward cylinder. Unlike the previous case, the boundary of this shadow can be determined in a straightforward, analytic raytracing process. The first step in this process is to parameterize the edge of the shadow. This boundary is a circle given by Eq. (44).

$$\partial \Omega_{w_3} = \mathbf{r}_{\text{middle panel}}\big|_{u_3 = r_2} \tag{43}$$

$$\partial \Omega_{w_3} = [-l_1, \quad r_2 \sin v_3, \quad r_2 \cos v_3]^{\mathsf{T}} \tag{44}$$

Mapping this boundary to the forward shadow using Eq. (33) results in the system of equations in Eqs. (45)-(47). This system can be used to isolate u_2 and v_2 and describe the shadow on the forward hull caused by the aft hull. This relationship between u_2 and v_2 is given by Eq. (48).

$$u_2 = l_1 + t \cos \alpha \tag{45}$$

$$r_1 \sin v_2 = r_2 \sin v_3 \tag{46}$$

$$r_1 \cos v_2 = r_2 \cos v_3 - t \sin \alpha \tag{47}$$

$$u_2(v_2) = l_1 - \cot \alpha \left(\sqrt{r_2^2 - r_1^2 \sin^2 v_2} + r_1 \cos v_2 \right) \tag{48}$$

The effect of self-shadowing can be incorporated by considering Eq. (48) to be a limit of integration in u. Unfortunately, after the u-integration of Eqs. (25) and (26), the v-integrals do not have closed-form solutions. Another issue with this definition of the shadow boundary arise when the shadow boundary intersects the natural bound on the cylinder. These issues are overcome by considering the extreme value of u on the shadow and eliminating the dependence on v. Substituting $\pi/2$ for v yields the result in Eq. (49). This approximation is also advantageous because the wetted area of the forward surface is approximated by a shorter cylindrical hull, a surface for which closed-form expressions have been previously derived and validated.

$$u_2(v_2) \approx u_2\left(\frac{\pi}{2} \right) = l_1 + \cot \alpha \sqrt{r_2^2 - r_1^2} \tag{49}$$

2. Biconic

The biconic geometry, shown in Figure 4(b), is defined in this investigation as a conical frustum that is followed by a second frustum. The parameterizations for each distinct surface on the biconic are given by Eqs. (51)-(57). Whether the cone angle of the aft frustum is greater than or less than that of the forward frustum will result in different shadow mappings. In the case where the cone angle increases, the forward

American Institute of Aeronautics and Astronautics

frustum casts a shadow onto the aft frustum and reflects air molecules onto it. For a decreasing cone angle, the two frustums can be superimposed without loss of fidelity because self-reflection cannot occur and the shadow from the first frustum is entirely contained within the shadow of the aft frustum.

$$\mathbf{r}_{\text{forward panel}} = [0, \quad u_1 \sin v_1, \quad u_2 \cos v_1]^{\mathsf{T}} \tag{50}$$

$$u_1 \in [0, r_0], v_1 \in [-\pi, \pi] \tag{51}$$

$$\mathbf{r}_{\text{forward frustum}} = [r_0 \cot \delta_{c_1} - u_2, \quad u_2 \tan \delta_{c_1} \sin v_2, \quad u_2 \tan \delta_{c_1} \cos v_2]^{\mathsf{T}} \tag{52}$$

$$u_2 \in [r_0 \cot \delta_{c_1}, r_1 \cot \delta_{c_1}], v_2 \in [-\pi, \pi] \tag{53}$$

$$\mathbf{r}_{\text{aft frustum}} = [r_1 \cot \delta_{c_2} - (r_1 - r_0) \cot \delta_{c_1} - u_3, \quad u_3 \tan \delta_{c_2} \sin v_3, \quad u_3 \tan \delta_{c_2} \cos v_3]^{\mathsf{T}} \tag{54}$$

$$u_3 \in [r_1 \cot \delta_{c_2}, r_2 \cot \delta_{c_2}], v_3 \in [-\pi, \pi] \tag{55}$$

$$\mathbf{r}_{\text{aft panel}} = [-(r_1 - r_0) \cot \delta_{c_1} - (r_2 - r_1) \cot \delta_{c_2}, \quad v_4 \sin u_4, \quad v_4 \cos u_4]^{\mathsf{T}} \tag{56}$$

$$u_4 \in [-\pi, \pi], v_4 \in [0, r_2] \tag{57}$$

For biconic geometries the integration across the forward conical frustum is the same, while the aft frustum integration varies. The forward conical frustum naturally shadows itself whenever the freestream angle is greater than its cone angle. This condition is given by Eq. (58), where the real function, Re, is used to eliminate the need for a conditional or piecewise function in the limits of integration. When the cone angle is greater than the freestream angle, the real part of the arccosine is identically π, so the limits of integration would be $-\pi$ and π. With the domain of integration defined by the shadow boundary, closed-form expressions for the aerodynamic coefficients of the forward conical frustum can be calculated.

$$v_2 = \pm \mathrm{Re} \left(\cos^{-1} \left(-\cot(\alpha) \tan \left(\delta_{c_1} \right) \right) \right) \tag{58}$$

In a biconic configuration, the forward frustum shadows onto the aft frustum when the freestream angle is greater than the cone angle of the forward cone. Applying the analytic raytracing technique from Eq. (33), the shadow on the aft cone is given by Eq. (59).

$$u_3 = \frac{\cot \left(\delta_{c_2} \right) \left(\cot \left(\delta_{c_2} \right) - \cot \left(\delta_{c_1} \right) \right) \left(r_0 \cot \left(\delta_{c_1} \right) + l_1 \right) \eta}{\cot \left(\delta_{c_2} \right) \cot \left(\delta_{c_1} \right) \eta - \sin(v_3) \cot^2 \left(\delta_{c_1} \right) + \cot(\alpha) \cos(v_3) \cot \left(\delta_{c_1} \right) \eta + \cot^2(\alpha) \sin(v_3)} \tag{59}$$

$$\eta = \sqrt{1 - \cot^2(\alpha) \tan^2 \left(\delta_{c_1} \right)} \tag{60}$$

The boundary of the shadow given by Eq. (59) describes a hyperbola. The shadow boundary on the forward conical frustum is linear and the normal vector along that boundary is constant, so there is a tangent plane along this shadow boundary. This plane intersects the aft conical frustum, generating a conic section, and due to the geometry of this problem that section is a hyperbola. This hyperbolic bound can be introduced into the u limits of integration, however the resulting v integral cannot be evaluated closed-form. To solve this problem, the parameter from Eq. (58) for the front frustum is used as the shadow boundary of the aft frustum. Geometrically, this approximation is significantly different from the exact hyperbolic solution in Eq. (59), however the area between the these two boundaries does not contribute significantly to the overall aerodynamic coefficients. Since the u-integration is unchanged under the asymptote approximation and the v-integration bounds are constants, the aerodynamic coefficients for the aft frustum can be derived in closed-form.

In the case of the decreasing biconic, where the aft cone angle is less than the forward cone angle, is more straightforward because two conical frustums can be superimposed without loss of fidelity in the model or geometry. The shadow from the forward frustum can be mapped onto the aft frustum using the analytic raytracing method and the result is that the mapped shadow is always contained within the natural shadow of the aft frustum. In this case, no hyperbolic approximation is necessary; the integration process for the aft frustum is identical to the process for the forward frustum. This result can be applied directly to any solid of revolution whose radius function has a monotonically decreasing slope. Geometries including paraboloids, oblate spheroids, ogives, and sphere-cones can all be discretized and summed by the trapezium formula to yield their aerodynamic coefficients.[22]

American Institute of Aeronautics and Astronautics

3. Arbitrary Axisymmetric Geometry

The methodology above for combining two shape primitives can be extended to any number of primitives to approximate an arbitrary axisymmetric geometry. For such shapes, the radius at a point on shape is a function of its axial position. Approximating this function with piecewise-constant values yields a stepped cylinder geometry. Using a piecewise-linear approximation to the radius function would yield a surface composed of conical frustums. Consider a surface of revolution defined by Eq. (61). The function f can be sampled at a list of u values, and between the samplings the function is approximately linear as shown in Eq. (62). Since the integral is a linear operator, the equations for the force and moment coefficients can be evaluated on the ith interval and summed to obtain an expression for entire surface.

$$\mathbf{r} = [u, f(u) \sin v_1, \quad f(u) \cos v_1]^\intercal \tag{61}$$

$$f(u) \approx \begin{cases} f_1 + \frac{u-u_1}{u_2-u_1}(f_2 - f_1) & u_1 \le u < u_2 \\ f_2 + \frac{u-u_2}{u_3-u_2}(f_3 - f_2) & u_2 \le u < u_3 \\ \dots & \dots \\ f_i + \frac{u-u_i}{u_{i+1}-u_i}(f_{i+1} - f_i) & u_i \le u < u_i + 1 \\ \dots & \dots \\ f_{n-1} + \frac{u-u_{n-1}}{u_n-u_{n-1}}(f_n - f_{n-1}) & u_{n-1} \le u < u_n \end{cases} \tag{62}$$

The assumptions made in generating the biconic and stepped cylinder equations tend to break down when there is a significant variation in the properties of each element. This approximation is appropriate for radius functions that are piecewise smooth and have a continuous derivative. More specifically, if the radius function has a monotonically decreasing derivative, then approximating the surface with a series of conical frustums will produce aerodynamic coefficients without a loss of model fidelity.

V. Validation Scheme

A. Rarefied Aerodynamic Coefficients

The expressions for the rarefied aerodynamic coefficients are validated primarily against Direct Simulation Monte Carlo (DSMC) numerical simulations. Experimental and reconstructed flight data supplant the DSMC results to validate analytic expressions for regularly parameterized surfaces. The NASA-developed DSMC Analysis Code (DAC) was used to perform the numerical simulations because it is an industry-accepted, high-fidelity rarefied gas flow simulator. Wind tunnel test results for the sphere are available and compared against the analytic expressions.

In the analytic expressions, there are at least eight independent factors that affect the aerodynamic coefficients. Varying each of these factors on ranges would be resource-intensive and wasteful if some of those factors do not significantly change the value of the coefficients. A nonlinear sensitivity analysis can provide information regarding which of the factors are most significant. The drag coefficient of a flat plate can be derived from Eq. (25) as a function of the orientation of the freestream, the momentum accommodation coefficients, the freestream velocity, temperature, and molar mass, and the wall temperature. These parameters lie on ranges, given in Table 1, while an object is in low-Earth orbit (LEO).

Bound	α_a (deg)	β_a (deg)	V_∞ (m/s)	T_∞ (K)	M (g/mol)	σ_N	σ_T	T_W (K)
	Input Variable							
Lower	-90	-90	5500	200	2	0	0	100
Upper	90	90	9500	2000	46	1	1	500

Table 1. Ranges for variables in sensitivity analysis.

Assuming independent uniform distributions on each of the factors, a Monte Carlo simulation on the gradient of the drag coefficient can be performed. These data are presented in Figure 5 as a probabilistic Pareto chart.[23] The results indicate that α, β, σ_N, and σ_T are the most often the significant variables. To validate geometries with planes of symmetry, the space of (α, β) can be reduced. Generally, since a purely

American Institute of Aeronautics and Astronautics

specular reflection has $\sigma_N = \sigma_T = 0$ and a purely diffuse surface has $\sigma_N = \sigma_T = 1$, there is some correlation between the two momentum accommodation coefficients. For the purpose of reducing the space of factors to vary, the same value on $[0, 1]$ is assigned to σ_N and σ_T. Other variables than the 8 in the flat plate drag coefficient will appear in the analytic expressions of different shapes, such as the length and diameter of a cylinder, but these are not swept in the validation of the analytic expressions of rarefied aerodynamic coefficients.
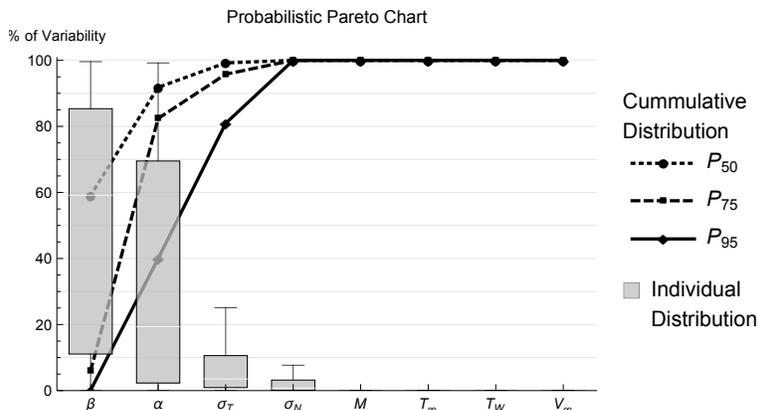
Figure 5. Nonlinear sensitivity analysis of the drag coefficient of a flat plate.

B. Solar Radiation Pressure

A combination of paneling and prior results are used to validate the analytic expressions for the perturbations due to SRP. Dividing Eqs. (27) and (28) by the solar radiation pressure, the results are area and volume vectors which are dependent only on the optical properties of the surface, the orientation of the object with respect to the Sun, and the geometry of the object. These quantities are varied on ranges, taking advantage of symmetries, and compared against panel approximations. This is an approximation because the integral over infinitely many infinitesimal surfaces is replaced by a sum of finite surfaces. The panel approximation does not include the effects of self-shadowing or self-shadowing, so the panel approximation will be more accurate for the convex geometries than for the stepped cylinder and increasing biconic.

The SRP perturbation expressions are functions of the geometry of the objects, the reflectivity and diffusivity of the surface, and the orientation of the solar vector. A sample geometry was generated for each shape and the optical properties and orientation parameters were varied on ranges. The set of simulations were determined by full factorial, but because the optical properties must sum to one, they were sampled from a triangular domain to enforce the relationship $\alpha + \rho + \delta = 1$.[18] The ranges and number of levels for each factor are shown in Table 2. The maxima of the orientation angles were adjusted for shapes with lines or planes of symmetry to prevent duplicate sampling.

	Input Variable			
	α_s (deg)	β_s (deg)	ρ	δ
Lower Bound	0	0	0	0
Upper Bound	180	180	1	1
Samples	11	11	11	11

Table 2. Ranges for variables in SRP validation simulations.

American Institute of Aeronautics and Astronautics

VI.   Analytic Model Validation

A.   Rarefied Aerodynamic Coefficients

1.   Sphere

The analytic expression for drag on a sphere was validated against both DAC numerical simulations and against experimental results. In Figure 6(a), the drag on a sphere is shown as computed by DAC and by the analytic model.[10] Figure 6(b) shows a comparison of the expression against wind tunnel test results.[24]


(a) DAC Comparison   (b) Experimental Comparison
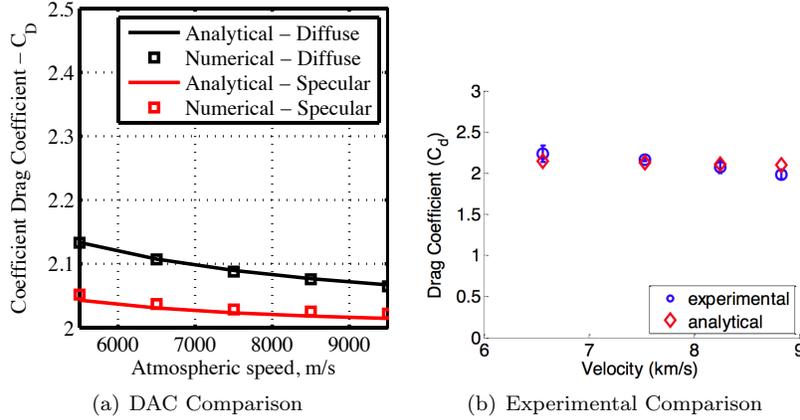
Figure 6.   Validation of the rarefied aerodynamic drag coefficient of a sphere.

2.   Cuboid

Analytic expressions for a cuboid were developed using the Heaviside formulation of the surface integral, described in Eq. (31). From the moment results in Figure 7, it appears that there is no net moment on the cuboid and that both the analytic and numerical results are sampling zero with some error when comparing the magnitudes of the moment coefficients with those for the cone in Figure 9.

(a) Axial Force   (b) Side Force   (c) Normal Force

(d) Rolling Moment   (e) Pitching Moment   (f) Yawing Moment
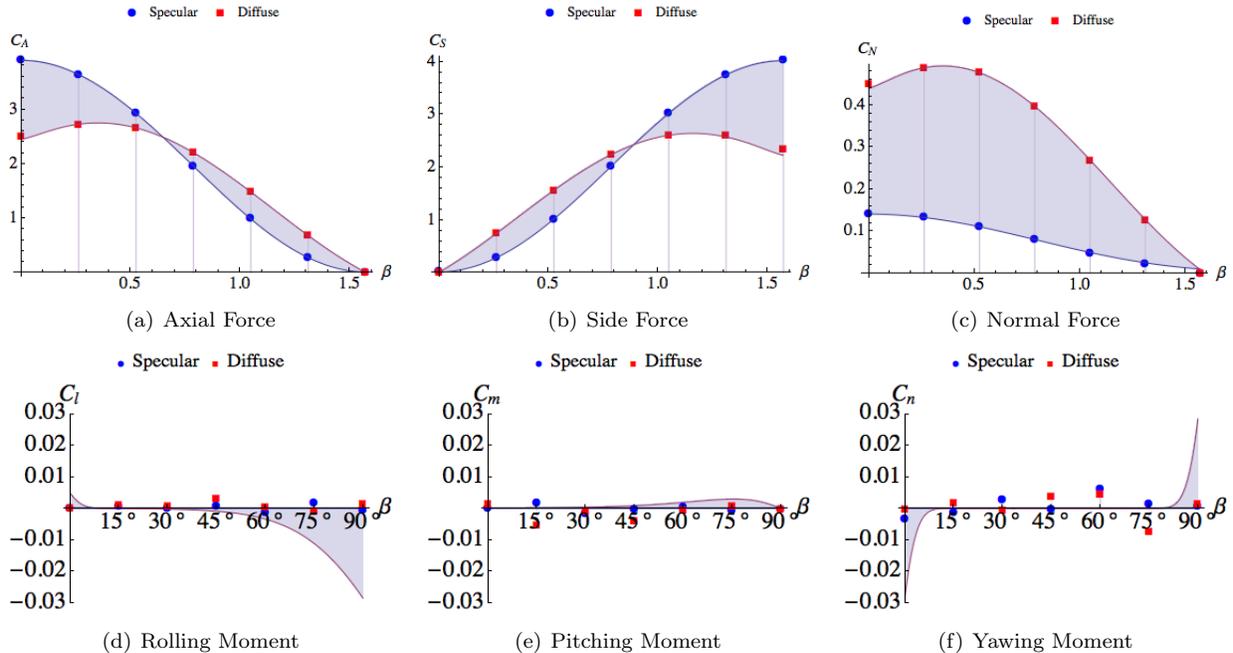
Figure 7.   Validation of the aerodynamic coefficients of a cuboid.

American Institute of Aeronautics and Astronautics

3. Cylinder

The analytic force and moment coefficients on the cylinder were derived by taking advantage of the axial symmetry of the body. This means that the freestream can be restricted to the body's (x, y)-plane, effectively collapsing the angle of attack (α) to zero and letting the side slip angle (β) vary on the interval $[0, \pi/2]$. Every freestream orientation can be x-rotated to lie in the first quadrant of the (x, y)-plane, so these results can be x-rotated to any other freestream orientation. The analytic results for a cylinder with a length-to-diameter ratio of 2.18 and with the side slip angle varied on the range $[0, \pi/2]$ are compared to DAC numerical simulation data in Figure 8. The two cases of specular and diffuse reflections are plotted together to illustrate the range of valid solutions which the analytical model can be applied.
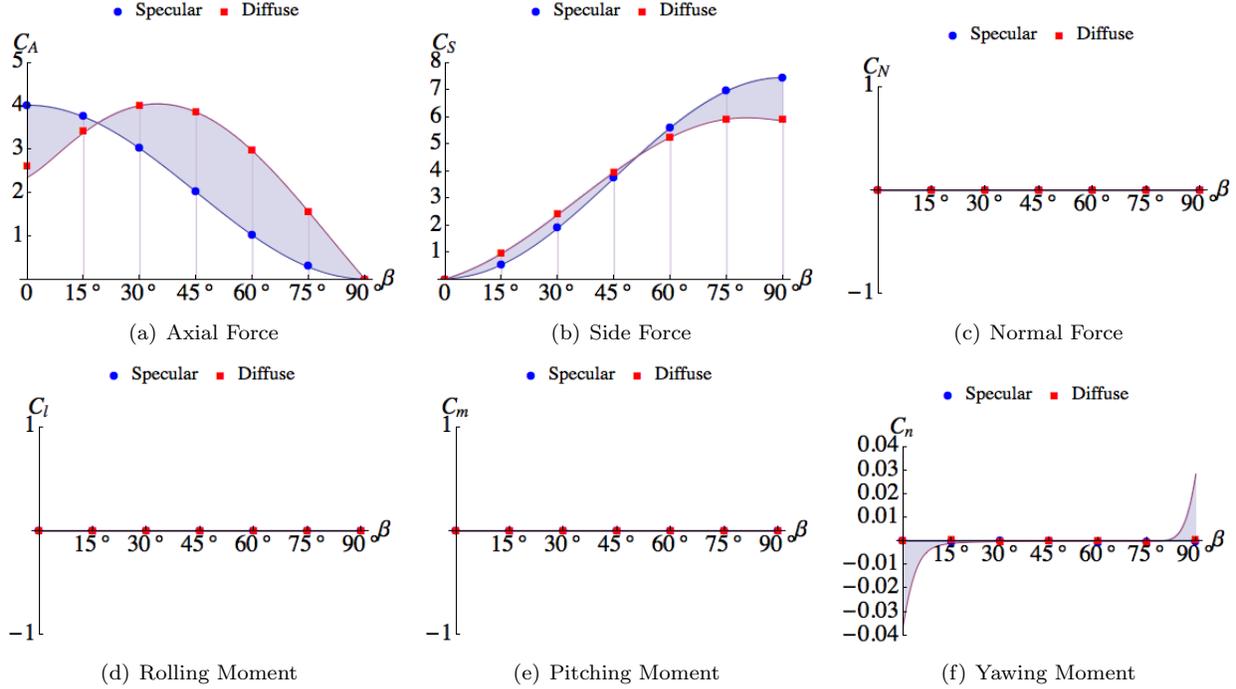
Figure 8. Validation of the aerodynamic coefficients of the cylinder.

The specular results show the most agreement between DAC and the analytic model, and in most cases this is also true of the diffuse results. The two models are different in cases where there is a small angle between the freestream and either the circular face or the hull of the cylinder. This effect is apparent in each of the above plots, and most noticeable in Figure 8(f). A small local freestream angle corresponds to significant tangential forces, which explains the "tails" on the yawing moment graph. The effect is also evident on the diffuse curves in the force coefficient graphs.

4. Cone

To validate the expressions for the cone, a sample case with a 36° was simulated in DAC and in the analytic expressions. The results for the cone are presented in Figure 9. Overall there is good agreement between the two solutions, with the most notable effect being the relative insensitivity to the accommodation coefficients at low angles of attack. Once the angle of attack passes the cone angle and shadowing occurs, the solutions for different accommodation coefficient values start to differ.

5. Ellipsoid

Both the angle of attack and the sideslip angle were varied to validated the ellipsoid equations. Since three parameters are varied simultaneously, the results from DAC and the analytic model are plotted against each other in Figure 10(a). Subtracting the analytic results from the DAC results yields the residuals in Figure 10(b). The ratio of the residual to the analytic result is illustrated in Figure 10(c). Histograms of the residual and the relative difference are given in Figures 10(d) and 10(e). Overall, the aerodynamic

American Institute of Aeronautics and Astronautics
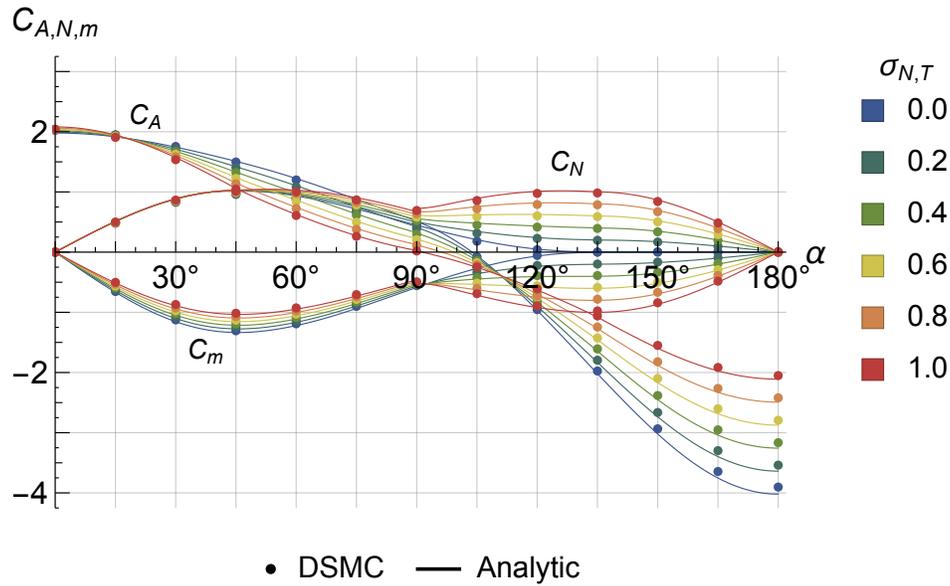
Figure 9. The rarefied aerodynamic coefficients of a $36°$ cone.

coefficients predicted by the analytic model are accurate to within 10% of the coefficients predicted by DAC. There are some outlying cases where the analytic model over-predicts the value of the normal coefficient, however in most cases there is a good agreement between the two models.

6. Stepped Cylinder

An aerodynamic database for the stepped cylinder shown in Figure 11 was generated using the analytic models and compared against DAC simulations. The plots show consistent agreement between the analytic model and DAC results. The model does not include self-reflection of molecules, a feature that is apparent in the axial force coefficient at angles of attack of $10° - 20°$. The difference between the analytic and numerical results is more significant for specular reflections. This effect is not apparent for diffuse molecular reflections, which is more common in nature. For diffuse reflections, self-shadowing is a more significant effect than self-reflection and the two models consistently predict the same values for the aerodynamic coefficients within a 5% difference.

7. Increasing Biconic

For the increasing biconic geometry shown in Figure 4(b), there is consistent matching of the DAC and analytic predictions in the case of diffuse reflections. In Figure 12, the effects of self-reflection are evident in the error plots at $20°$, $150°$, and $160°$. The magnitude of the error decreases as the accommodation coefficient increases. For diffuse reflections, the analytic and DAC results are within 5% difference. The analytic model also accurately predicts the angles of attack where the coefficients become invariant to the accommodation coefficient, best illustrated in the axial force coefficient plot.

8. Decreasing Biconic

Strong agreement between the analytic and DAC results is shown in Figure 13 for the decreasing biconic geometry. The geometry detailed in Figure 4(c) was analyzed as a representative example. At all angle of attacks and accommodation coefficients, the analytic equations predict aerodynamic coefficients that are consistent with the DAC simulations up to 5%. Of the three elemental superpositions of geometric

American Institute of Aeronautics and Astronautics
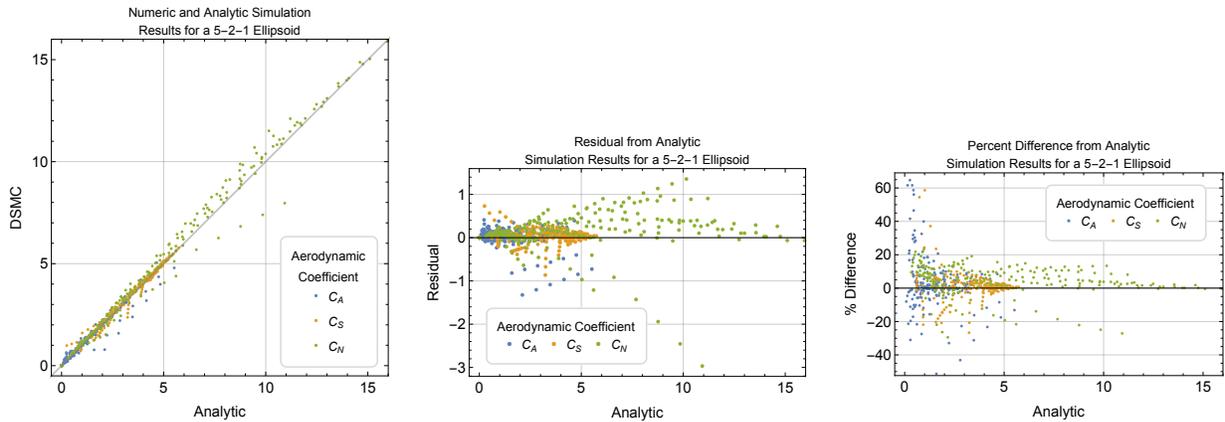
(a) Actual vs Predicted   (b) Residual vs Predicted   (c) Percent Difference vs Predicted
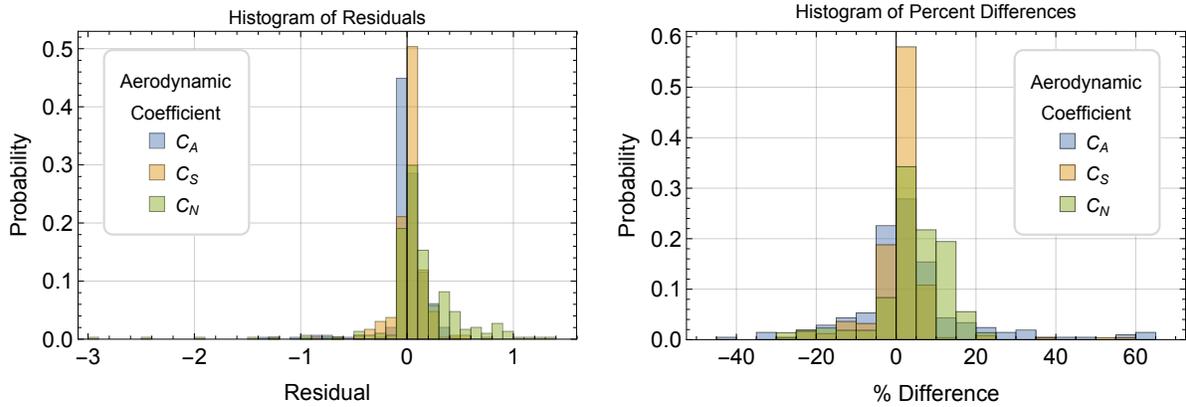
(d) Residual Distribution   (e) Percent Difference Distribution

Figure 10. Simulation results for the aerodynamic coefficients of an ellipsoid.
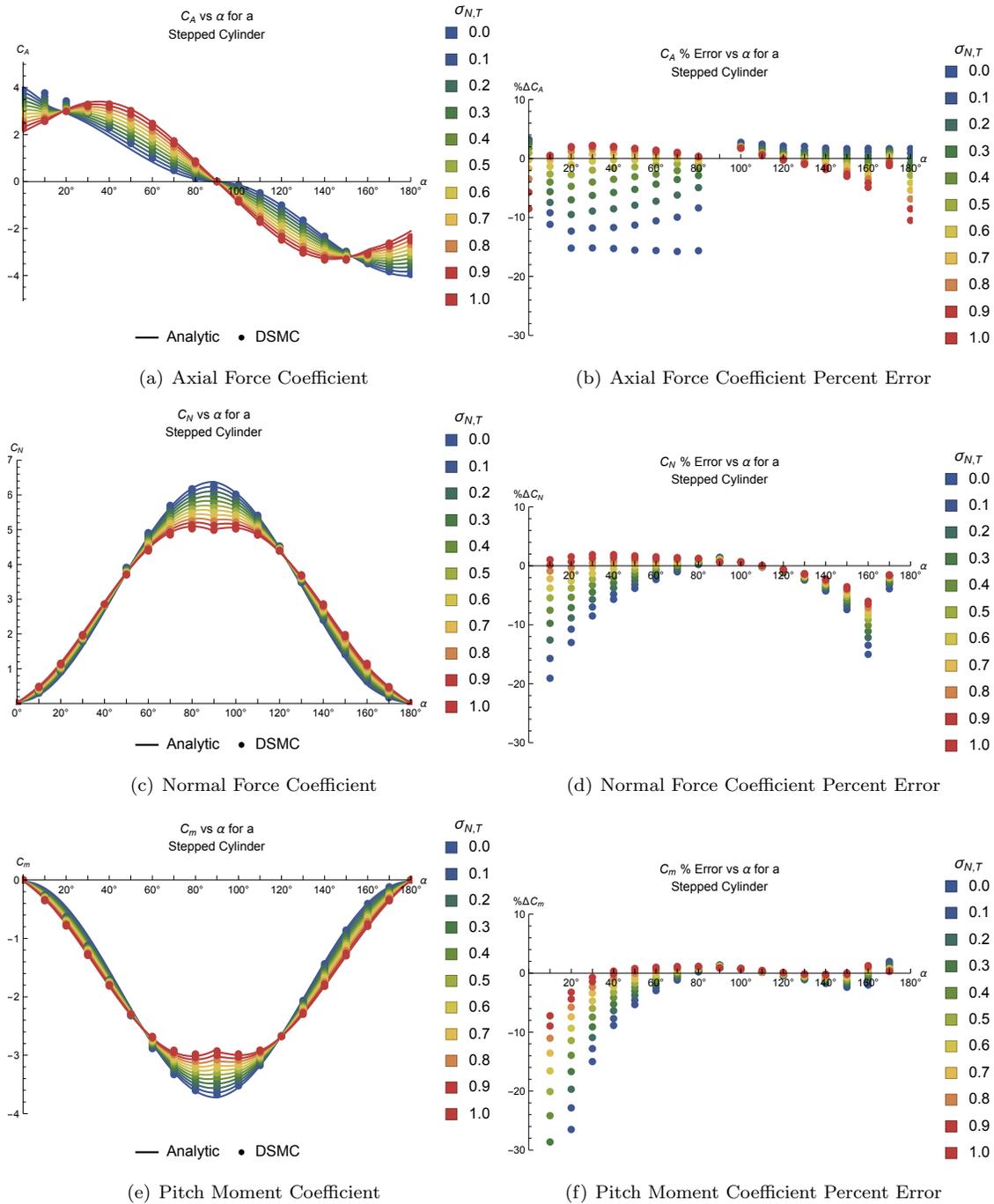
Figure 11. Comparison of Analytic and DAC estimates of the rarefied aerodynamic coefficients of a stepped cylinder.

primitives, the decreasing biconic is the most promising candidate for the basis of modeling an arbitrary surface of revolution.

9. Arbitrary Conic

The formulation for the arbitrary surface of revolution is applied to the Mars Microprobe aeroshell, shown in Figure 4(d). The analytic model is compared in Figure 14 against published DSMC results.[21]

American Institute of Aeronautics and Astronautics

(a) Axial Force Coefficient

(b) Axial Force Coefficient Percent Error

(c) Normal Force Coefficient

(d) Normal Force Coefficient Percent Error

(e) Pitch Moment Coefficient

(f) Pitch Moment Coefficient Percent Error
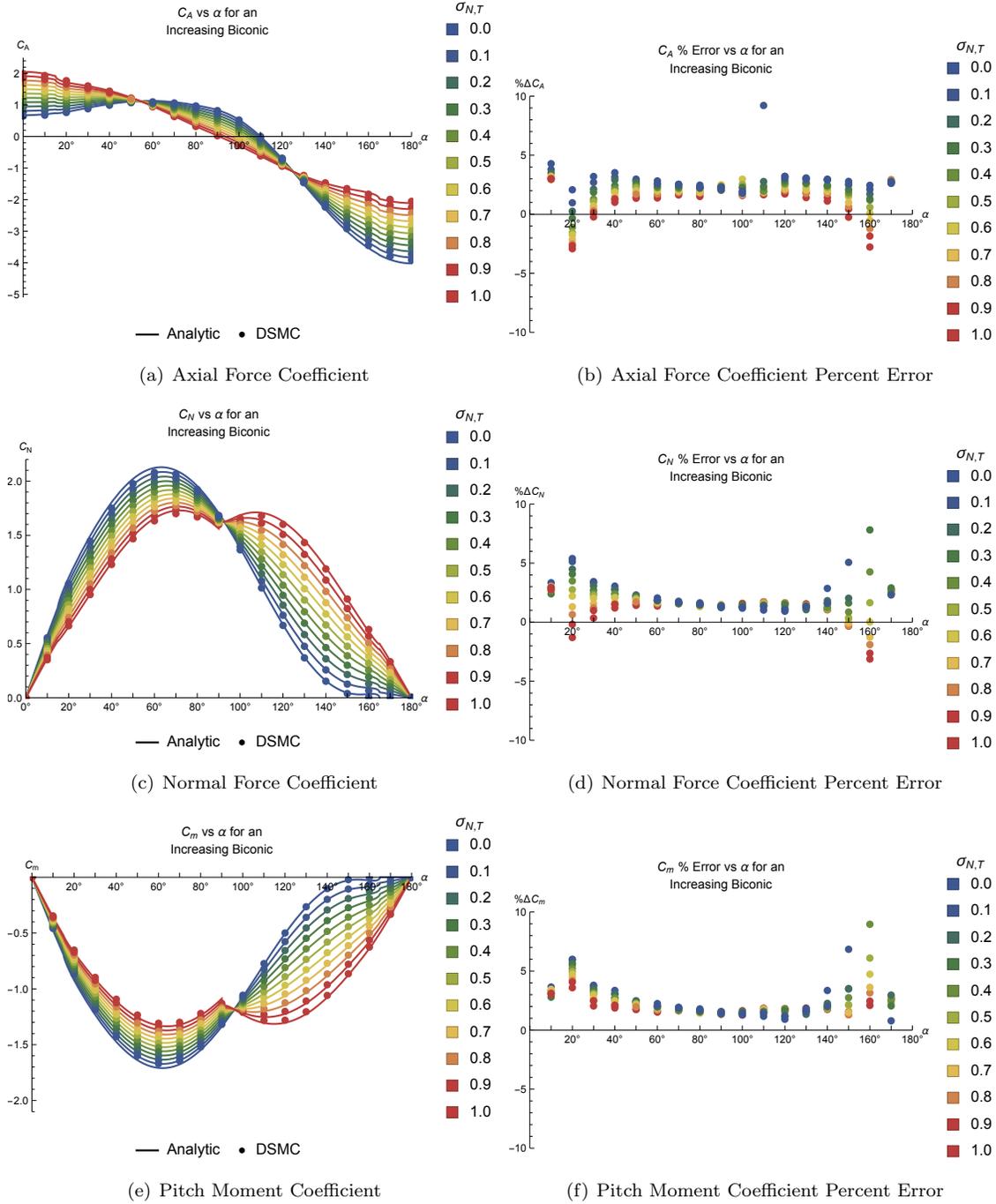
Figure 12. Analytic and DAC estimates for the aerodynamic coefficients of an increasing biconic.

B. Solar Radiation Pressure

1. Sphere

Analytic integration of Eq. (27) has been previously performed for the sphere and the resulting expression for the drag on a sphere, shown in Eq. (63) matches with the literature.[19]

$$D_s = \frac{\Phi_\odot}{c} \left(\frac{4}{9}\delta + 1 \right) \pi r^2 \tag{63}$$

(a) Axial Force Coefficient   (b) Axial Force Coefficient Percent Error

(c) Normal Force Coefficient   (d) Normal Force Coefficient Percent Error

(e) Pitch Moment Coefficient   (f) Pitch Moment Coefficient Percent Error
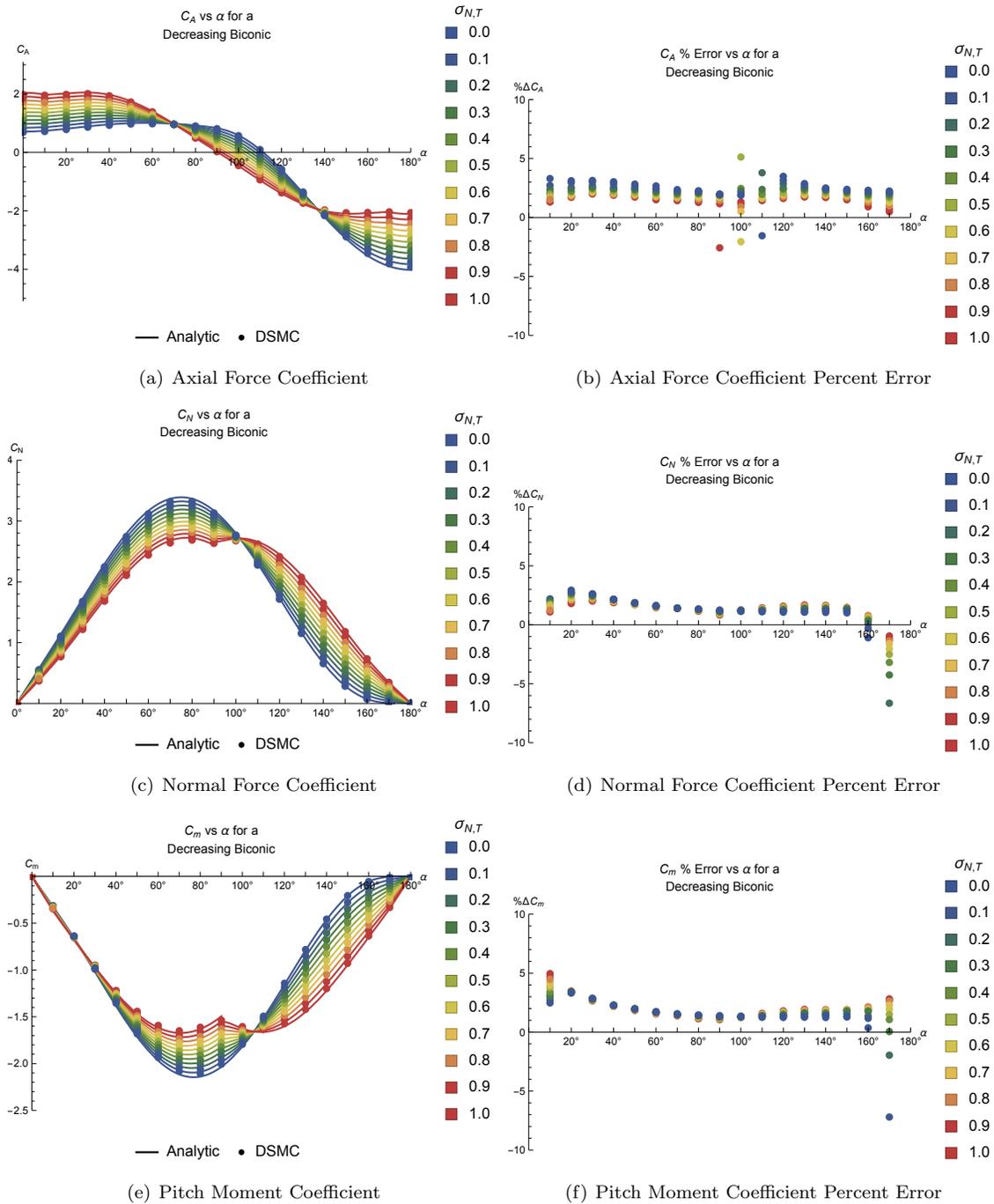
Figure 13. Aerodynamic coefficients of a decreasing biconic as predicted by the analytic solution and DAC.

2. Cuboid

The panel approximation is exact for a cuboid, explaining the agreement between the two models in Figure 15. The axial term is plotted but not shown because the other two force terms are overplotted. Solar radiation pressure generates no moments on the cuboid.

3. Cylinder

There is excellent agreement between the analytic and approximate multipliers for SRP on a cylinder, with all the values agreeing to within 0.6% between the two models. There are no moments about the center of

American Institute of Aeronautics and Astronautics

(a) Axial Force Coefficient

(b) Axial Force Coefficient Percent Error

(c) Normal Force Coefficient

(d) Normal Force Coefficient Percent Error

(e) Pitch Moment Coefficient

(f) Pitch Moment Coefficient Percent Error
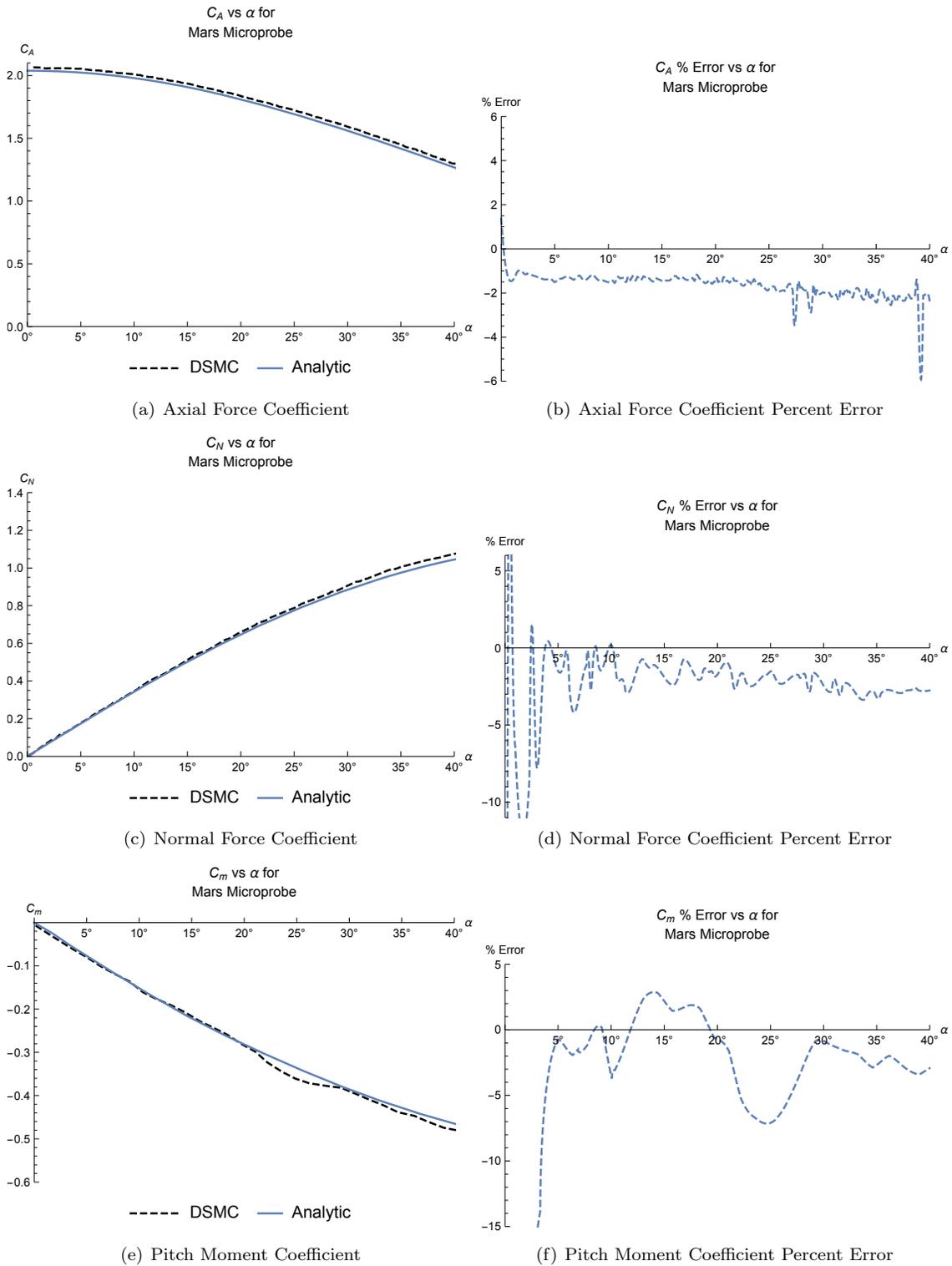
Figure 14. Analytic and DSMC curves for the rarefied aerodynamics of the Mars Microprobe aeroshell.[21]

(a) Actual vs Predicted

(b) Residual vs Predicted
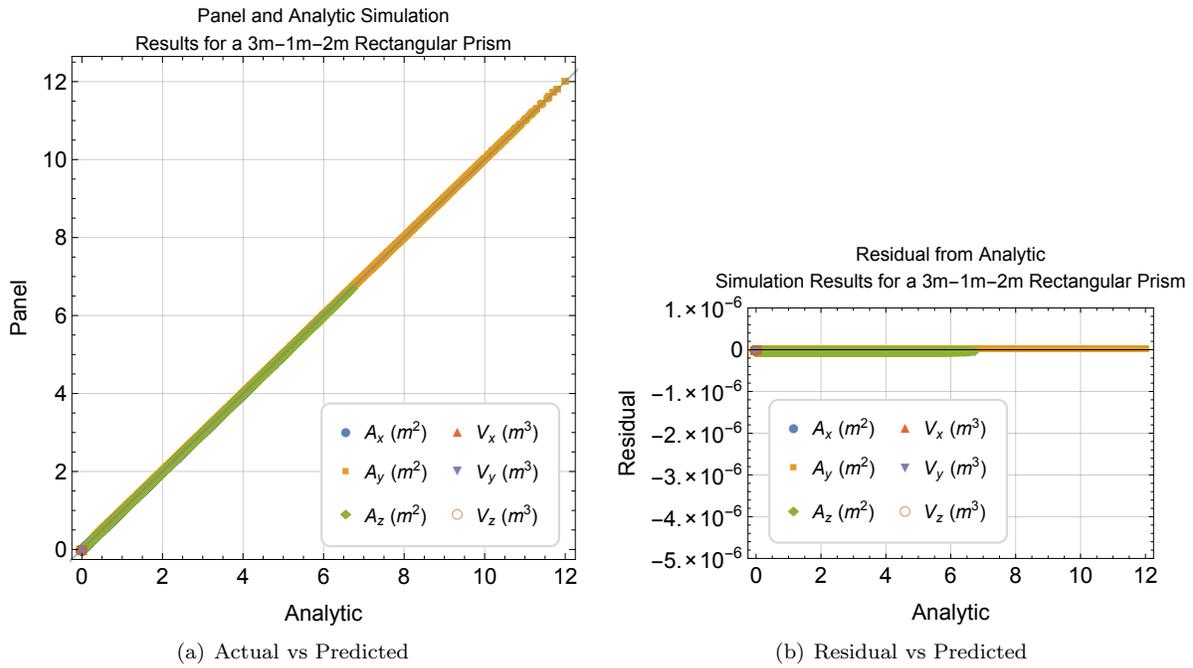
Figure 15. Simulation results for the SRP multipliers of a cuboid.

the cylinder generated by SRP.

(a) Actual vs Predicted

(b) Residual vs Predicted

(c) Percent Difference vs Predicted
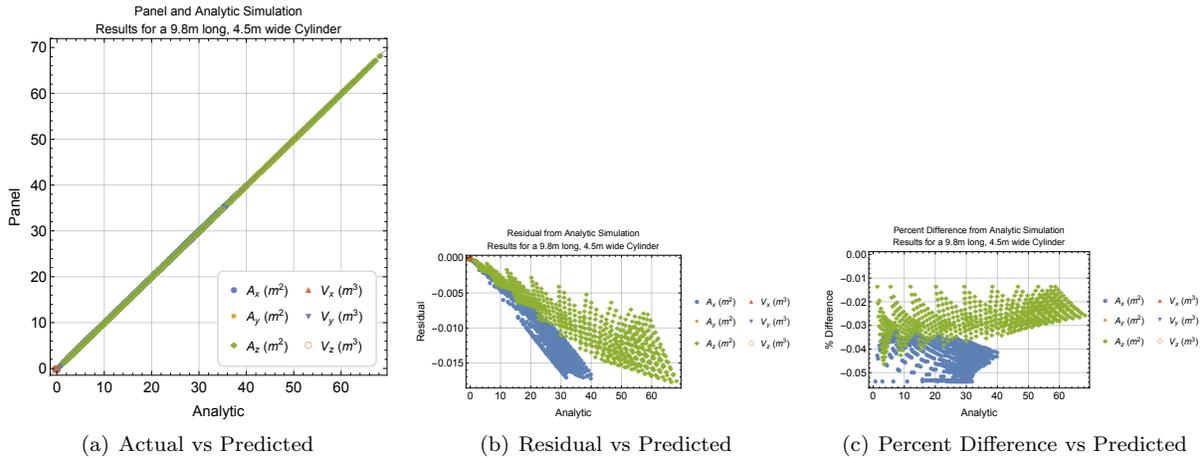
Figure 16. Simulation results for the solar radiation pressure multipliers of a cylinder.

4. Cone

Presented in Figure 17 are the simulation results for the solar radiation pressure on a cone. The panel approximation agrees with the analytic expressions to within 0.1%.

5. Ellipsoid

The analytic model for the SRP perturbation on a 5m-2m-1m ellipsoid is compared against the panel results in Figure 18. The analytic model does not predict a moment on the ellipsoid due to SRP, however the panel approximation predicts very small moment values. This discrepancy suggests that there are net moments on an ellipsoid, however because the ellipsoid is paneled there is a slightly non-zero value predicted. This results is consistent with the DAC simulations for the rarefied aerodynamics of an ellipsoid: the analytic model predicted no moments by symmetry and the DSMC results showed slightly nonzero moments.

American Institute of Aeronautics and Astronautics

(a) Actual vs Predicted   (b) Residual vs Predicted   (c) Percent Difference vs Predicted
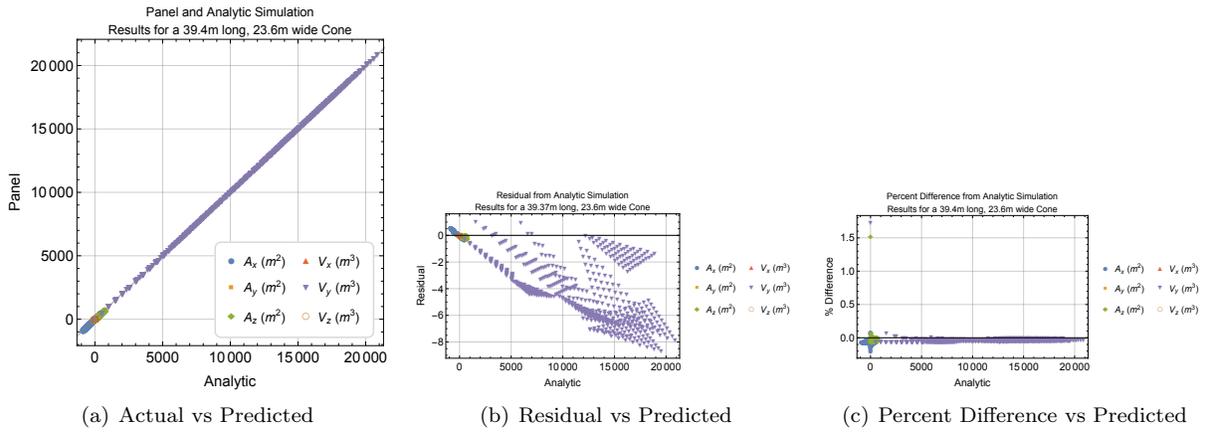
Figure 17. Simulation results for the SRP multipliers of a cone.

(a) Actual vs Predicted   (b) Residual vs Predicted
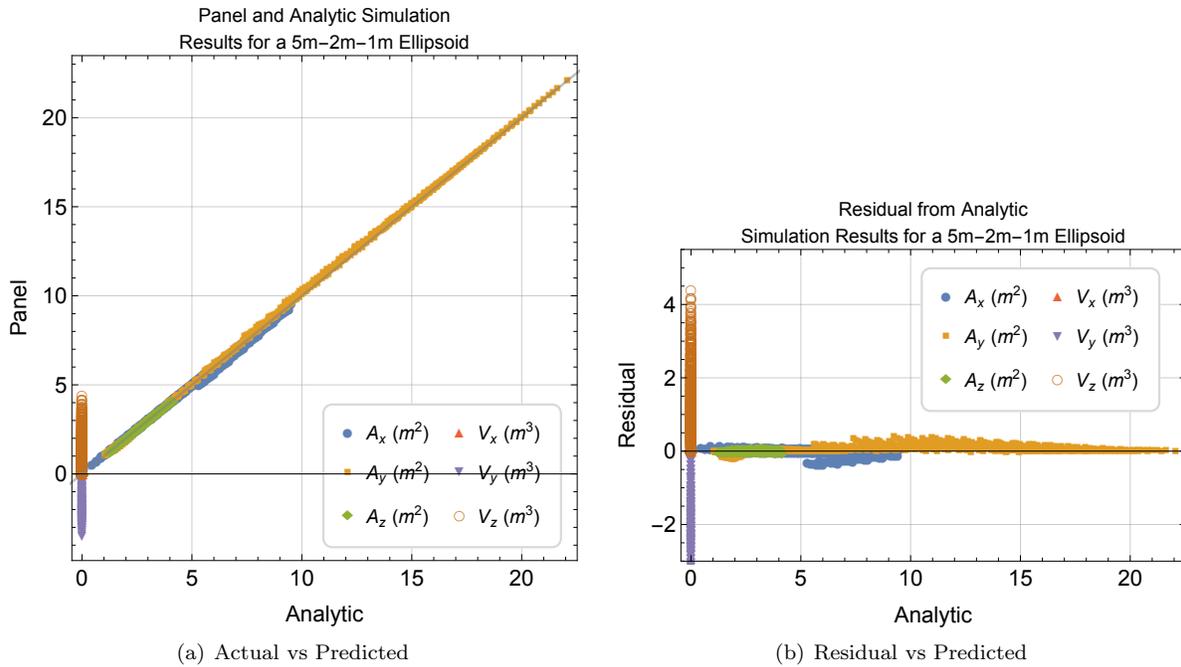
Figure 18. Simulation results for the SRP multipliers of an ellipsoid.

American Institute of Aeronautics and Astronautics

6. Stepped Cylinder

The stepped cylinder results are provided in Figure 19 and show very good agreement between the panel and analytic models. There is more error between the two models in this geometry compared to the previous geometries because the panel model does not account for self-shadowing or self-reflection phenomena.


(a) Actual vs Predicted   (b) Residual vs Predicted   (c) Percent Difference vs Predicted
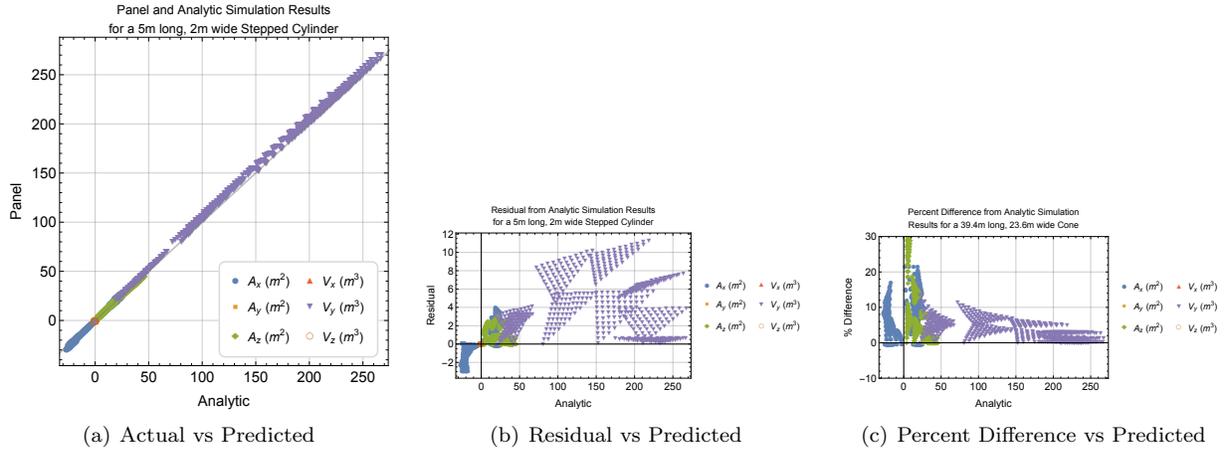
Figure 19. Simulation results for the SRP multipliers of a stepped cylinder.

7. Increasing Biconic

The two models for the increasing biconic agree with each other to within 5% as shown in Figure 20. As with the stepped cylinder, the primary difference between the two models is that self-shadowing is not included in the panel approximation.


(a) Actual vs Predicted   (b) Residual vs Predicted   (c) Percent Difference vs Predicted
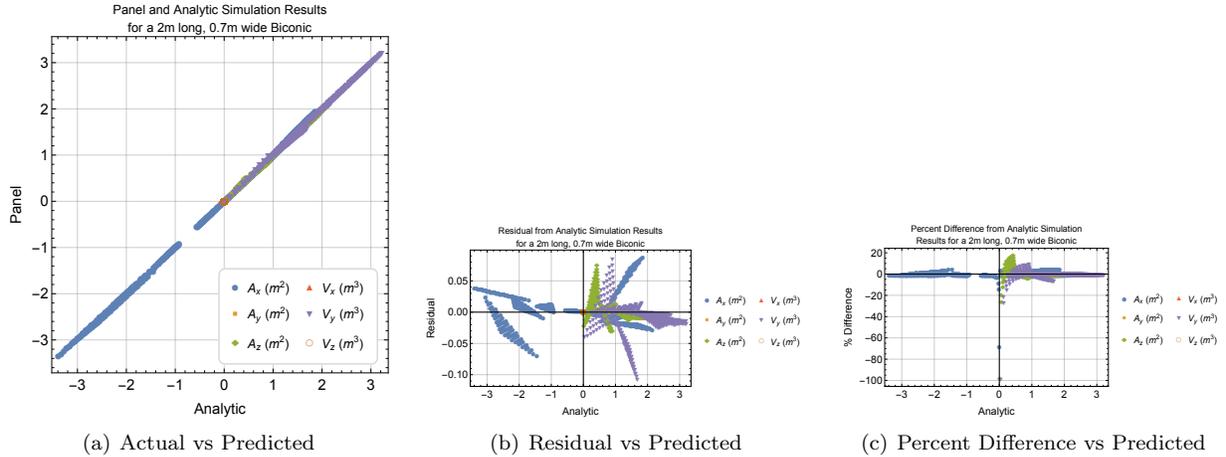
Figure 20. Simulation results for the SRP multipliers of an increasing biconic.

8. Decreasing Biconic

The decreasing biconic is a convex shape, resulting in no self-shadowing considerations. Without self-shadowing, this geometry shows better agreement between the two models as shown in Figure 21 compared to the increasing biconic.

VII. Application

An example use case for analytic, high-fidelity modeling of these perturbations is propellant-less maneuvering in LEO. Nanosatellites have recently proliferated in LEO due to their affordability, however propulsion

American Institute of Aeronautics and Astronautics

(a) Actual vs Predicted   (b) Residual vs Predicted   (c) Percent Difference vs Predicted
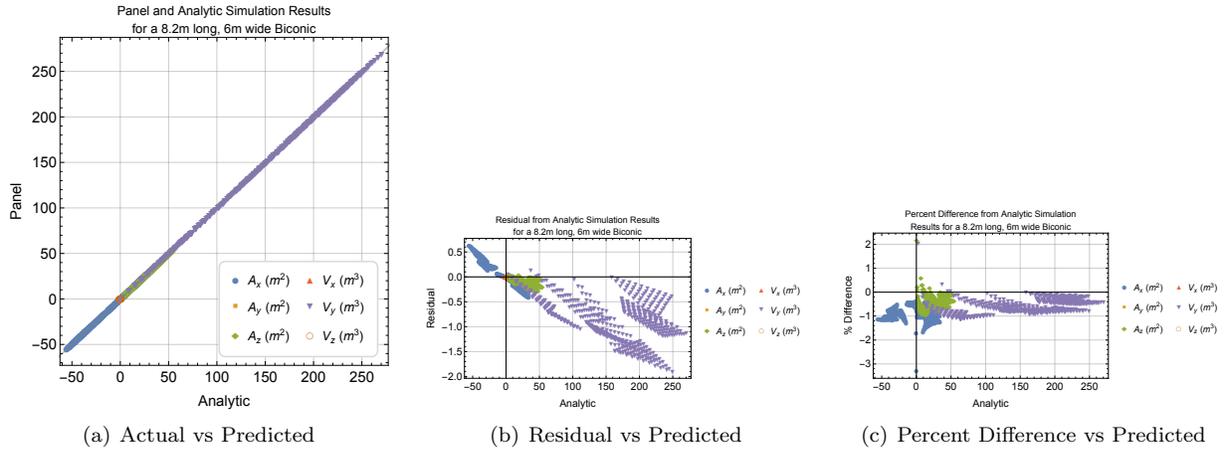
Figure 21. Simulation results for the SRP multipliers of a decreasing biconic.

systems have been limited to cold gas thrusters. A representative 3U nanosatellite, shown in Figure 22, has a flap on the prograde face which can be set to an angle ϕ. The impact of this angle on the orbital elements of the nanosatellite are examined by generating analytic aerodynamic force equations, and propagating them over several orbits. For this case study a spherical Earth with exponential atmosphere is assumed and the initial orbit is 250km circular. The satellite is also assumed to have a fixed attitude in the LVLH frame and exhibit purely diffuse molecular reflections.
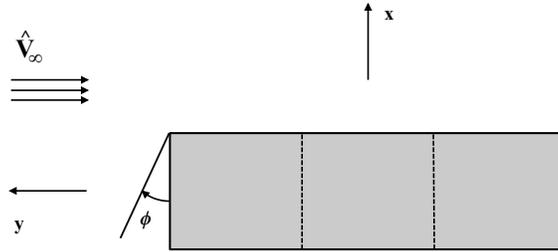

Figure 22. Diagram of case study nanosatellite.

The analytic aerodynamic force coefficients for this geometry were generated by modifying the equations for a rectangular prism. The windward face of the geometry was split into two segments: the flap and the exposed base of the satellite. With an exponential atmosphere and circular orbit, the freestream dynamic pressure can be expressed in terms of the nanosatellite's altitude. Given that the aerodynamic force is expressed in the local frame, the trajectory of the satellite is expressed in terms of the planar orbital elements using Gauss's variational equations. These equations are propagated with a variable order Adams-Bashforth-Moulton PECE solver. Taking the closed flap case, $\phi = 0$, as the nominal trajectory, the distance from this trajectory was calculated for several flap angles and shown in Figure 23. These results show that the distance from nominal grows approximately 13 cm/day at a flap angle of 10 degrees, 30 cm/day at 20 degrees, 38 cm/day at 30 degrees, and 40cm/day at 40 degrees. There is a brief reduction in the dispersions at approximately 30 days indicating an approach to the nominal trajectory. This phenomenon is caused by the conflicting short-term and long-term effects of aerodynamic drag on the phase angle. In the short term, the decrease in drag causes the satellites to move ahead in the orbit, however in the long term the trailing satellite will have a shorter period, so it will speed up relative to the leading satellite and close the distance between them. Though the quoted dispersion rates imply a linear growth in the distance from the nominal case, the growth rate will increase on the timescale of years when the differences in orbital periods dominates.

The trajectory of a nanosatellite with a prograde-facing flap is relatively insensitive to the angle that flap makes with the body. Overall, the aerodynamic perturbations on this nanosatellite are minor, especially considering the host of non-spherical gravity perturbations that act on the satellite, a result that may be useful in the design or troubleshooting of nanosatellite GN&C.

American Institute of Aeronautics and Astronautics
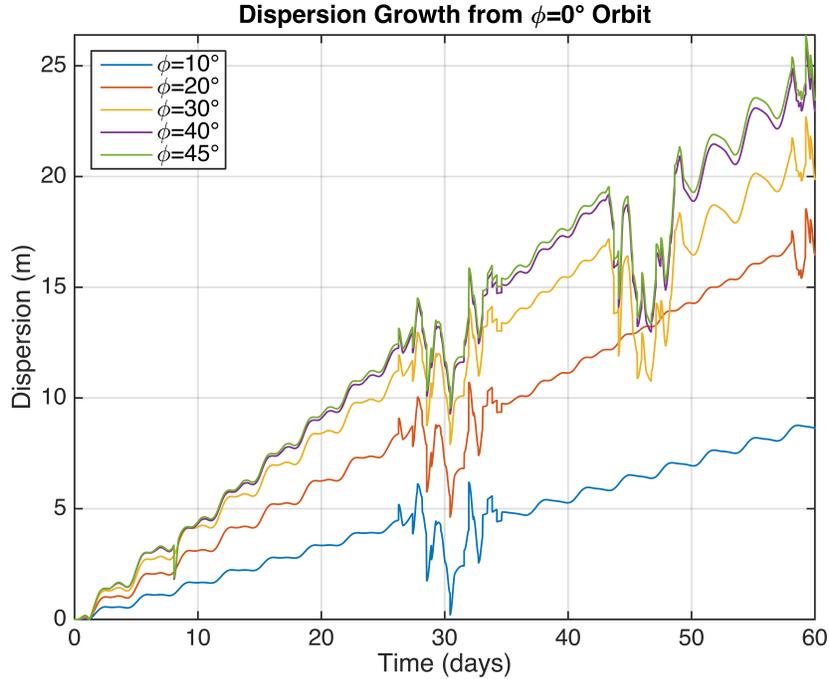
Figure 23. The dispersion history for various flap angles. The results are symmetric about $\phi = 45°$, so the history for $20°$ is the same as for $70°$.

VIII. Summary

As the number of tracked RSOs, it is important to develop fast high-fidelity models of non-gravitational perturbations. Using rarefied aerodynamic and SRP point force models and integrating them over the wetted surface with a computer algebra system has yielded analytic models of these perturbations that are as accurate as numerical simulations with significantly reduced computation time. Analytic modeling was limited to primitive shapes, described by relatively simple parameterizations, however through superposition these models are extensible to the modeling composite geometries. The aerodynamic model was used to determine the dispersion evolution for a 3U nanosatellite and illustrate the competing short term and long term effects of differential aerodynamics.

IX. Future Work

The parameterization of the ellipsoid used in this investigation results in analytic expressions which require significant computation expense to evaluate. One possibility for reducing the complexity of the expressions is to consider isometric projections of the wetted region and treating these elliptical projections as flat plates. These ellipses would not generally be aligned with the coordinate axes, requiring a series of linear transformations to recover unit circle domains of integration. These transformations may result in numerically ill-conditioned expressions at grazing angles. Future work regarding the superposition framework would be validation against non-axisymmetric geometries and determination of its limits of applicability without self-reflection. Another consideration with the superposition framework is the $\mathcal{O}(n^2)$ growth rate that may result in expressions that require more computational resources than DSMC, where n is the number of unique surfaces. The value of n where this tradeoff occurs should be quantified in the future to determine the limits of analytic modeling. The analytic models developed for the SRP perturbations should be compared, in the future, against numerical simulation tools such as a raster image Monte Carlo code.

Acknowledgments

References

[1] *The Space Report 2014*, The Authoritative Guide to Global Space Activity, The Space Foundation, Colorado Springs, CO, 2014.

[2] Nielsen, P. D., Alfriend, K. T., Bloomfield, M. J., Emmert, J. T., Guo, Y., Maclay, T. D., Miller, J. G., Morris, R. F., Moore, A. B., Russell, R. P., Saari, D. G., Scheeres, D. J., Schonberg, W. P., and Sridharan, R., "Continuing Kepler's Quest," Tech. rep., National Research Council, Washington, DC, 2012.

[3] Grant, M. J. and Braun, R. D., "Analytic Hypersonic Aerodynamics for Conceptual Design of Entry Vehicles," *48th AIAA Aerospace Sciences Meeting Including the New Horizons Forum and Aerospace Exposition*, American Institute of Aeronautics and Astronautics, Orlando, Jan. 2010.

[4] Grant, M. J. and Braun, R. D., "The Extension of Analytic Hypersonic Force Coefficients for Conceptual Design Using the Divergence Theorem," *AIAA Atmospheric Flight Mechanics Conference*, 2012.

[5] Grant, M. J., "The Construction of Analytic Hypersonic Pitch Moment Coefficients Using a Curl Transformation," *51st AIAA Aerospace Sciences Meeting*, American Institute of Aeronautics and Astronautics, Dallas, TX, 2013.

[6] Regan, F. J. and Anandakrishnan, S. M., *Dynamics of Atmospheric Re-Entry*, American Institute of Aeronautics and Astronautics, Reston, VA, 1993.

[7] Sentman, L. H., "Free Molecule Flow Theory and Its Application to the Determination of Aerodynamic Forces," Tech. rep., Lockheed Missiles & Space Company, Sunnyvale, CA, Oct. 1961.

[8] Schaaf, S. A. and Chambré, P. L., "Flow of Rarefied Gases," Princeton University Press, Princeton, NJ, 1961.

[9] Stalder, J. R. and Zurick, V. J., Tech. Rep. NACA-TN-2423, National Advisory Committee for Aeronautics, Moffett Field, CA, July 1951.

[10] Hart Jr, K. A., Dutta, S., Simonis, K. R., and Steinfeldt, B. A., "Analytically-derived Aerodynamic Force and Moment Coefficients of Resident Space Objects in Free-Molecular Flow," *AIAA Atmospheric Flight Mechanics Conference, National Harbor, MD*, Jan. 2014.

[11] Pratt, M. J., "Concave surfaces in free molecule flow," *AIAA Journal*, Vol. 1, No. 7, 1963, pp. 1716–1717.

[12] Schamberg, R., "On Concave Bodies in Free Molecule Flow," The RAND Corporation, 1967.

[13] Vallander, S. V., "Collection 1," *Aerodinamika Razrezhennykh Gazov*, 1963.

[14] Garfunkel, I. M., "Generalization of Applications of Free Molecule Flow," Tech. Rep. UMR4213, University of Michigan, Ann Arbor, MI, 1950.

[15] Boettcher, R. D. and Legge, H., "Determination of Aerodynamic Forces on Satellites by Theory and Wind-Tunnel Experiments," *Acta Astronautica*, Vol. 7, No. 3, 1980, pp. 255–267.

[16] Hart Jr, K. A., Simonis, K. R., Steinfeldt, B. A., and Braun, R. D., "Analytical Aerodynamic Force and Moment Coefficients of Axisymmetric Objects in Rarefied Flow," *AIAA Atmospheric Flight Mechanics Conference*, American Institute of Aeronautics and Astronautics, Kissimmee, FL, Jan. 2015.

[17] Hurlbut, F. C., *Encyclopedia of Applied Physics*, chap. Rarefied-Gas Dynamics, Wiley-VCH Verlag GmbH & Co KGaA, 2003, pp. 97–115.

[18] Milani, A., Nobili, A. M., and Farinella, P., *Non-Gravitational Perturbations and Satellite Geodesy*, Taylor & Francis, Jan. 1987.

[19] Früh, C., Kelecy, T. M., and Jah, M. K., "Coupled orbit-attitude dynamics of high area-to-mass ratio (HAMR) objects: influence of solar radiation pressure, Earth's shadow and the visibility in light curves," *Celestial Mechanics and Dynamical Astronomy*, Vol. 117, No. 4, 2013, pp. 385–404.

[20] Do Carmo, M. P., *Differential Geometry of Curves and Surfaces*, Prentice-Hall, Englewood Cliffs, NJ, 1976.

[21] Mitcheltree, R. A., Moss, J. N., Cheatwood, F. M., Greene, F. A., and Braun, R. D., "Aerodynamics of the Mars Microprobe Entry Vehicles," *Journal of Spacecraft and Rockets*, Vol. 36, No. 3, May 1999, pp. 392–398.

[22] Hildebrand, F. B., *Introduction to Numerical Analysis*, Second Edition, Courier Corporation, April 2013.

[23] Hart Jr, K. A., Steinfeldt, B. A., and Braun, R. D., "Formulation and Applications of a Probabilistic Pareto Chart," *56th AIAA/ASCE/AHS/ASC Structures, Structural Dynamics, and Materials Conference*, American Institute of Aeronautics and Astronautics, Kissimmee, FL, Jan. 2015.

[24] Maldonado, C. A. and Ketsdever, A. D., "Drag Measurements in a Simulated Low-Earth Orbit Environment," *53rd AIAA Aerospace Sciences Meeting*, American Institute of Aeronautics and Astronautics, Kissimmee, FL, Jan. 2015.